Geothermal mapping and remote sensing of surface thermal anomalies at Grændalur area, Hveragerði, SW Iceland

Patrick Muanza Kant

Faculty of Earth Sciences
University of Iceland
2021

Geothermal mapping and remote sensing of surface thermal anomalies at Grændalur area, Hveragerði, SW Iceland

Patrick Muanza Kant

60 ECTS thesis submitted in partial fulfillment of a
Magister Scientiarum degree in Geology

Advisors
Prof. Ingibjörg Jónsdóttir
Sigurður G. Kristinsson
Gunnlaugur M. Einarsson

Master's Examiner
Grímur Björnsson

Faculty of Earth Sciences
School of Engineering and Natural Sciences
University of Iceland
Reykjavik, September 2021

Geothermal mapping and remote sensing of surface thermal anomalies at Grændalur area, Hveragerði, SW Iceland

Remote sensing at Grændalur valley

60 ECTS thesis submitted in partial fulfillment of a *Magister Scientiarum* degree in Geology

Faculty of Earth Sciences
School of Engineering and Natural Sciences
University of Iceland
Askja, Sturlugötu 7
107, Reykjavik
Iceland

Telephone: 525 4000

Bibliographic information:
Patrick Muanza Kant, 2021,
Geothermal mapping and remote sensing of surface thermal anomalies at Grændalur area, Hveragerði, SW Iceland, Master's thesis, Faculty of Earth Sciences, University of Iceland, pp. 81.

Printing: Háskólaprent
Reykjavik, Iceland, September 2021

Abstract

The Grændalur Valley is located in southwest Iceland, immediately north of the town of Hveragerði. It is located at the contact of the eastern margin of the Western Volcanic Zone (WVZ) and the South Icelandic Seismic Zone (SISZ). The area is seismically active, the most recent significant earthquake swarm occurred on May 29, 2008 with magnitudes of 6.3 and 5.5 between the towns of Selfoss and Hveragerði. The Grændalur valley is one of the areas in the Hveragerði region with intense geothermal activity. Geothermal mapping has been carried out in this area to map surface geothermal manifestations such as hot and warm springs, mud pools, fumarole, steam vents, steaming ground and structures. Remote optical sensors (Landsat and ASTER satellite images) were used to identify thermal anomalies in this area. The analysis of thermal anomalies made on daytime and nighttime satellite images from 2005 to 2020 has detected a new geothermal activity in the north near the center that would have certainly been created after the earthquakes of May 29, 2008. The thermal infrared (TIR) image taken with a TIR camera carried by a DJI Matrice 200 drone with a Zenmus XT thermal camera at 120 m height, was compared with temperature measurements taken directly on the ground after the flight to calibrate the TIR image for accuracy. The TIR image was used to identify and estimate the surface temperature of a geothermal manifestation whose accessibility was difficult. The surface temperature of this geothermal manifestation is about 43°C.

Útdráttur

Í Grændal við Hveragerði er virkt hverasvæði og nokkur jarðskjálftavirkni, enda liggur dalurinn á mörkum vesturgosbeltisins og Suðurlandsbrotabeltisins. Öflug skjálftahrina gekk yfir svæðið vorið 2008, er skjálftar að stærð 6,3 og 5,5 M riðu yfir, en upptök þeirra voru á milli Selfoss og Hveragerðis.

Markmið verkefnisins var að kortleggja ummerki jarðhita í Grændal, svo sem leir- og gufuhveri, yfirborðsvatn og jarðfræðilega formgerð, og kanna jafnframt hvort vísbendingar væri að finna um breytingar á virkni svæðisins vegna skjálftahrinunnar 2008.

Ýmsum fjarkönnunargögnum var beitt við rannsóknina: Úr gervitunglum (LANDSAT, ASTER), loftmyndum (Loftmyndir ehf., Samsýn ehf.) og dróna (Matrice), en jafnframt var farið í vettvangsferð um svæðið. Greining hitamynda úr gervitunglum, frá tímabilinu 2005-2020, sýndi myndun nýrra hverasvæða í kjölfar skjálftanna 2008. Hitakortlagning var unnin með gögnum úr dróna DJI M200 dróna með Zenmuse XT hitamyndavél úr 120 m hæð, og kvörðuð með mælingum af jörðu niðri. Yfirborðshiti reyndist vera um 43°C.

Table of Contents

List of Figures

List of Tables

Abbreviations

EM : Electromagnetic energy

EGS : Enhanced Geothermal System

EMR : Electromagnetic radiation

EMS : Electromagnetic Spectrum

ETM : Enhanced Thematic Mapper

EVZ : Eastern Volcanic Zone

GPS : Global Positioning System

LST : Land Surface Temperature

MIR : Middle InfraRed

NVZ : North Volcanic Zone

OLI : Operational Land Imager

SISZ : South Iceland Seismic Zone

TIR : Thermal InfraRed

WVZ : Western Volcanic Zone

Acknowledgements

Sincere thanks goes to the government of the Democratic Republic of Congo through the Director General of the Geological and Mining Research Center (CRGM) for granting me the opportunity that made this study possible. Many thanks should go to the Icelandic Government through Director Guðni Axelsson, to all the staff of GRO-GTP for the financial support which made my stay and my studies at the University of Iceland possible and to Anette K. Mortensen for her advice that allowed me to give the best of myself for this thesis. I express my sincere gratitude to Lúdvík Georgsson for trusting me with this great opportunity.

I sincerely thanks to my supervisors Ingibjörg Jónsdóttir, Sigurður G. Kristinsson and Gunnlaugur M. Einarsson for the knowledge they imparted to me and the time they spent in making the valuable comments which enabled me to improve this research and this manuscript. I would like to wholeheartedly thank my examiner Grímur Björnsson for his questions, comments and suggestions.

I am indebted to the Congolese community in Iceland and all Icelandic friends who supported me a lot and made my stay in Iceland livable. I would like to thank the GRO-GPT fellows for the great time spent together.

My heartfelt thanks goes to my wife Mireille Masengu for her advice, her love, her affection, and the patience demonstrated throughout my study. A big thanks to my parents François Kant and Bilema Gode as well as to my brothers and sisters Jonathan Bamulumba, Cleberg Kant, Emilie Misengabu, Sylvie Meta, Danny Mbombo, Yvon Kazadi and Naomie Kuwa for your advice and prayers. May God bless you all abundantly.

1 Introduction

1.1 General overview

The Grændalur valley is one of the geothermal fields of the Hengill Central volcano and it is located about 6 km north of Hveragerði town (Fig.1). The Hveragerði town is located about 45 km southeast of Reykjavik, the capital of Iceland. The Grændalur valley is in the Southern Iceland Seismic Zone (SISZ) mainly in its western part which is in contact with the western flank of the active plate boundary between the North American and Eurasian crustal plates.

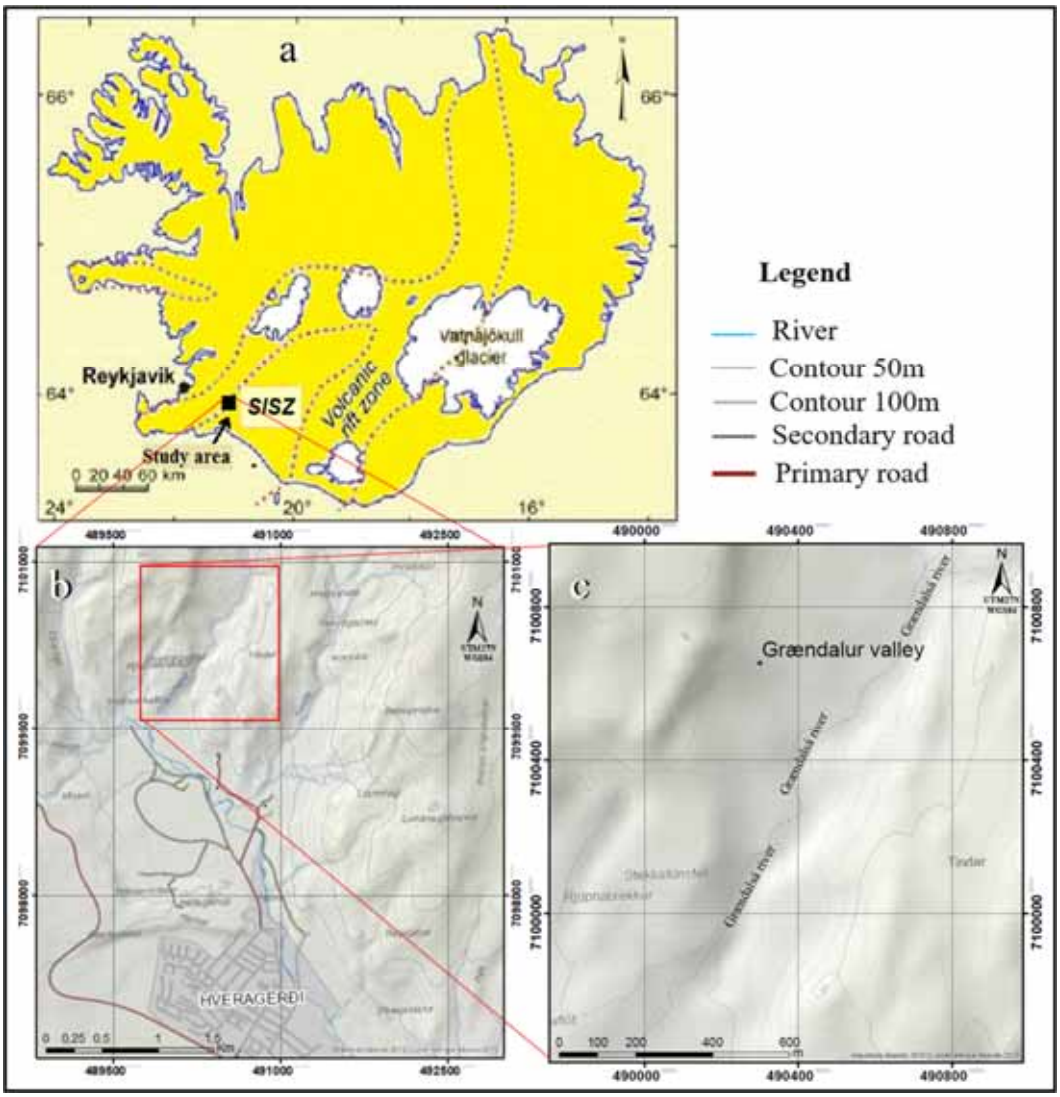

Figure 1: (a) General map of Iceland showing Reykjavik and study area. (b) Location of Hveragerði town and Grændalur area. (c) Location of Grændalur valley (Source: Esri).

In the Grændalur valley, geothermal activity is directly linked to the extinct Grændalur central volcano. This volcano is part of the Hengill volcanic system and has moved away from the center of the rift by the extension of the plate boundaries. This is one of the parts of the Hengill volcanic zone (Ingólfsson et al., 2008; Arnórsson, 1995a).

This study focuses on mapping surface geothermal manifestations and identifying thermal anomalies using thermal sensors. For geothermal mapping, the description and temperature measurement of geothermal manifestations were done in the field. For thermal analysis, we used thermal infrared (TIR) images obtained from satellites and drones. The analysis of the satellite images covering the period from 2005 to 2020 allowed us to identify the evolution of thermal anomalies in the Grændalur valley before and after the earthquake of May 2008.

In a geothermal area, the technique of processing the spatial resolution of the sensors described below using color images from different acquisition dates and DEM image for structures makes it possible to analyze the surface activity. It is a technique that can cover large areas and be applied in places where access is difficult. And the results of repeating this technique provide important information on the possible change at the surface that may be caused by geothermal activity. In this study, the results of this technique have allowed us to improve our knowledge of the evolution of geothermal activity in the Grændalur valley.

Currently in the world, the acquisition of images using drones has become essential and has increased. In this study, we used the drone for the acquisition of TIR images in a part of our study area. These images were then calibrated to provide us with estimated values of the surface temperature of the study area. Currently, the technology of using the drone can contribute significantly to the monitoring as well as the study of geothermal areas especially in areas where the accessibility seems to be difficult or dangerous.

1.2 Research objectives

1.2.1 General objective

To map geothermal manifestation and to identify surface thermal anomalies in Grændalur valley by using thermal infrared.

1.2.2 Specific objectives

The specific objectives of this research are to:

- map all surface geothermal manifestations
- identify thermal anomalies by using thermal infrared data from satellite images and a camera carried on a drone.

1.2.3 Research questions

- How can we map surface geothermal manifestation?

- How can we identify thermal anomalies by using thermal infrared data from satellite images and thermal infrared camera carried on a drone?

1.2.4 Hypothesis

- The identification, description, and collection of GPS coordinates of geothermal manifestations can allow us to map surface geothermal manifestations.

- The kinetic temperature of the earth's surface extracted directly from satellite images can reveal thermal anomalies. The analysis of images from different acquisition times can allow us to reconstruct the history of the evolution of thermal anomalies of a region and the high spatial resolution data from a thermal infrared camera carried on a drone can be used to identify and estimate the temperature in places where accessibility is difficult. This combination of techniques also allows for detailed mapping using color images and DEM for structures as well as monitoring of geothermal areas exposed to progressive changes.

2 Study area

2.1 Geological setting of Iceland

Iceland is an elevated plateau that lies in the middle of the North Atlantic between Norway and Greenland 63°23'N and 66°30'N, and ~12 – 25°W. It covers about 350,000km^2, about 103,000 km^2 above sea level with a crust thickness of 10-14km (Thórdarson and Larsen, 2007; Thórdarson and Höskuldsson, 2002). Iceland is located at the junction of the Greenland-Iceland-Faeroes Ridge which would be the Icelandic Hotspot Trail and the submarine Mid-Atlantic Ridge which is considered to be the constructive plate boundary between the Eurasian and American Plates (fig.2).

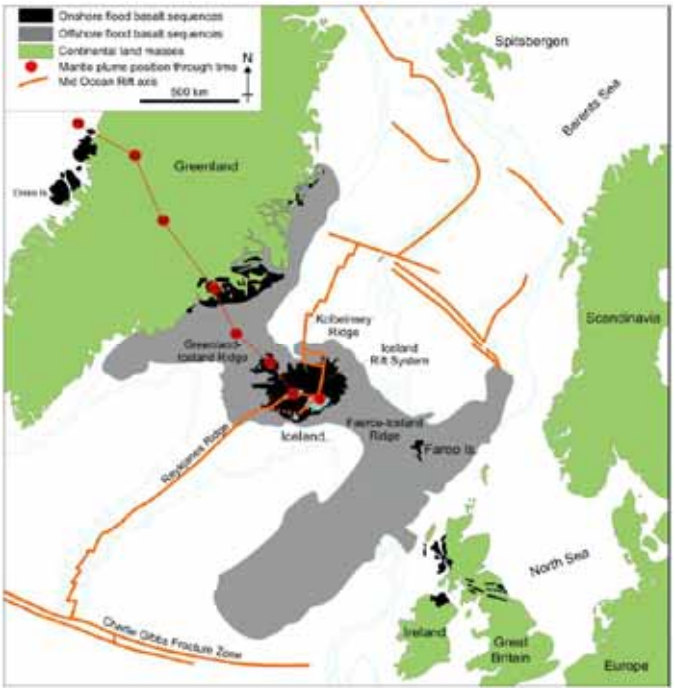

Figure 2: Regional geology of Iceland. The axis of the Mid-Atlantic Ridge is shown in heavy solid line. The dots with numbers represent the position of the mantle plume from 65 million years to the present (Thórdarson and Larsen, 2007).

The Icelandic basalt plateau is geologically young, and all of its rocks have formed over the past 25 million years. It rises more than 3000 m above the surrounding ocean floor (Thórdarson and Höskuldsson 2002). It is mainly composed of Holocene lavas (<0.01 Ma), subglacial hyaloclastites (0.01-0.78), Plio-Pliocene lavas (0.78-3 + 3 Ma) (Hardarson et al., 2008), and Tertiary plateau lavas (3.3-16 Ma) (Moorbath et al., 1968; Watkins and Walker, 1977; McDougall et al., 1984; Hardarson et al., 1997).

In Iceland, the main geological structures are volcanic systems. These systems are characterized by a volcanotectonic structure comprising a swarm of fissures and central volcano that cross the country (fig.3). In each volcanic system, fissure swarms are represented by faults and open fissures that are aligned following to the host volcanic zone. The central volcanoes are the focal point of eruptive activity (Thórdarson and Larsen, 2007). In the country, there are two transcurrent slip zones and several rift zones. In the south of

the country, the Reykjanes segment of the Mid-Atlantic Ridge comes on the shore at the Reykjanes Peninsula as an oblique rift zone and branches into the Western Volcanic Zone (WVZ) and through the South Iceland seismic zone (SISZ) oriented EW (Saemundsson, 1978). The Western Volcanic Zone (WVZ) is connected to the Eastern Volcanic Zone (EVZ) which extends northward and continues like the North Volcanic Zone (NVZ) through the South Icelandic Seismic Zone (SISZ) which is an EW transformation movement (Árnadóttir et al., 2008) (fig.3).

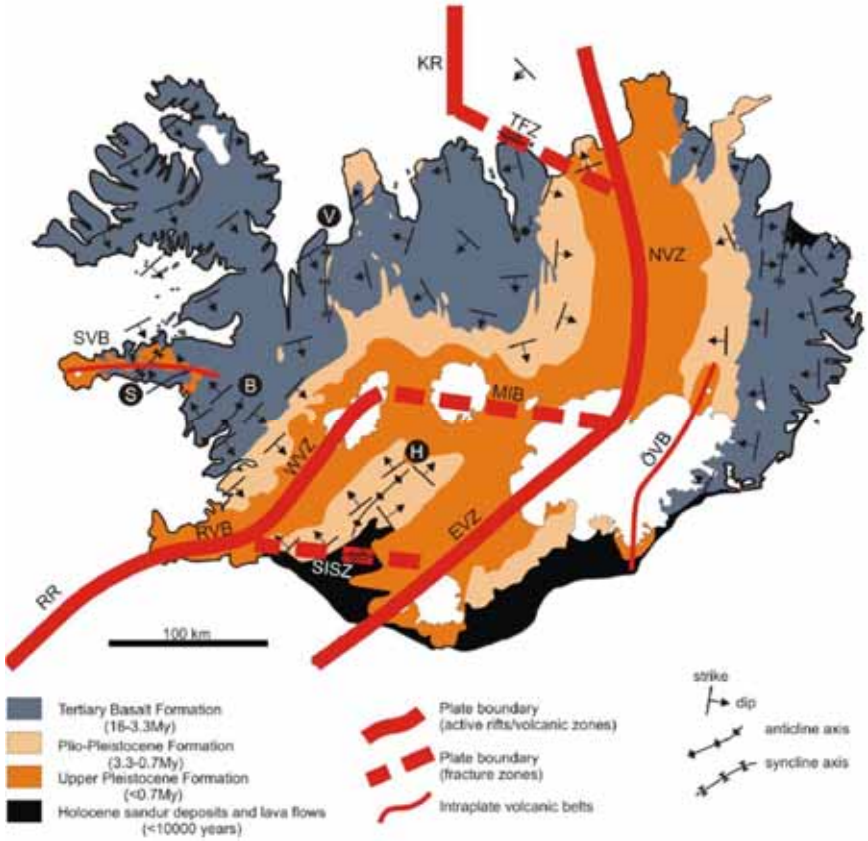

Figure 3: The principal elements of the geology in Iceland, outlining the distribution of the major geological subdivisions, including the main fault structures and volcanic zones and belts. RR, Reykjanes Ridge; RVB, Reykjanes Volcanic Belt; WVZ, West Volcanic Zone; MIB, Mid-Iceland Belt; SISZ, South Iceland Seismic Zone; EVZ, East Volcanic Zone; NVZ, North Volcanic Zone; TFZ, Tjörnes Fracture Zone; KR, Kolbeinsey Ridge; ÖVB, Öræfi Volcanic Belt; and SVB, Snæfellsnes Volcanic Belt. Letters enclosed by filled black circles indicate axes of anticlines and synclunes refered to in the text, where B and H indicate the Borgarfjörður and Hreppar anticlines and S and H the Snæfellsnes and Víðidalur synclines. From Thórdarson and Larsen (2007).

These volcanic systems, characterized by volcanic activity with the fissure swarms are directly related to the geothermal activity of Iceland (Bodvarsson, 1961; Gudmundsson and Jacoby, 2007; Thórdarson and Larsen, 2007). The geothermal systems in Iceland have been classified according to the temperature of the reservoir (Arnórsson et al., 2008; Axelsson et al., 2005; Bodvarsson, 1961; Fridleifsson, 1979); there are:

- low temperature systems (<150°C) are associated with fractures and faults, some of which are located in active fissure zones which cross obliquely the country and in older formations.

- high temperature systems (> 200°C) are located in the central parts of volcanic systems and in the region of central volcanoes (fig.4).

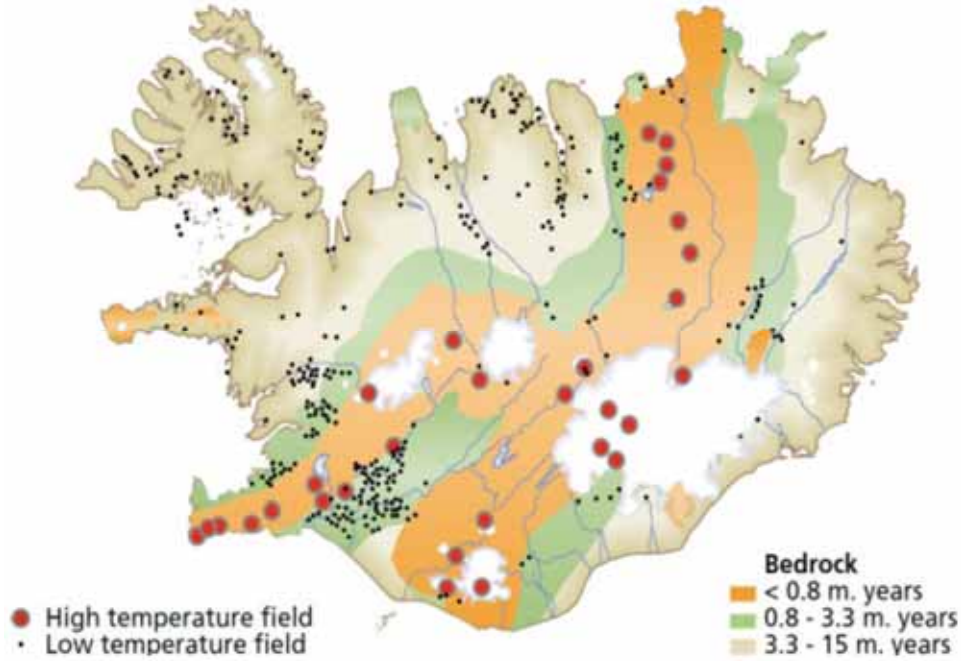

Figure 4: A simplified geological and geothermal map of Iceland (compiled by Saemundsson and Jóhannesson (2007), from Ragnarsson (2015)).

2.2 South Iceland Seismic Zone (SISZ)

The active volcanic rift zone in Iceland is divided into parallel branches towards the south (fig.5b). Between the two branches, there is a block which does not show any sign of active deformation, nor of volcanism and even less the epicenters of earthquake (Einarsson, 2008). This block is called Hreppar, it meets the criteria of a microplate and its lower limit towards the south is marked by the South Iceland Seismic Zone (SISZ) which is the seat of strike-slip earthquakes (Einarsson, 2008). These different zones are places of intense seismic activity and regular earthquakes (fig.5a). About 30 periods of destructive earthquakes have been recorded in SISZ since 1164 AD. The South Iceland Seismic Zone (SISZ) releases the stress accumulated during strike-slip earthquakes of about magnitude 7 (Einarsson, 1991). A large earthquake of magnitude 7 occurred in the area in 1912 and two earthquakes of magnitude 6.5 in 2000 on June 17 and 21, respectively (Pedersen et al., 2003). These various earthquakes in the area have increased geothermal activity (Björnsson G. and al., 2001). It is a phenomenon that occurs at intervals of decades to centuries.

The East-West-trending South Southern Iceland Seismic Zone (SISZ) shows evidence of Holocene fracturing and geologic formations such as alluvial plains, glacial surfaces and postglacial lava flows which are all fractured along this zone of 15 km wide and 70 km long (Einarsson and Eiríksson, 1982; Einarsson et al., 1981, 2002; Clifton and Einarsson, 2005). The majority of the fractures in this zone are oriented NNE to NE and form echelon fracture left-stepping to the left with a northern trend (fig.5a).

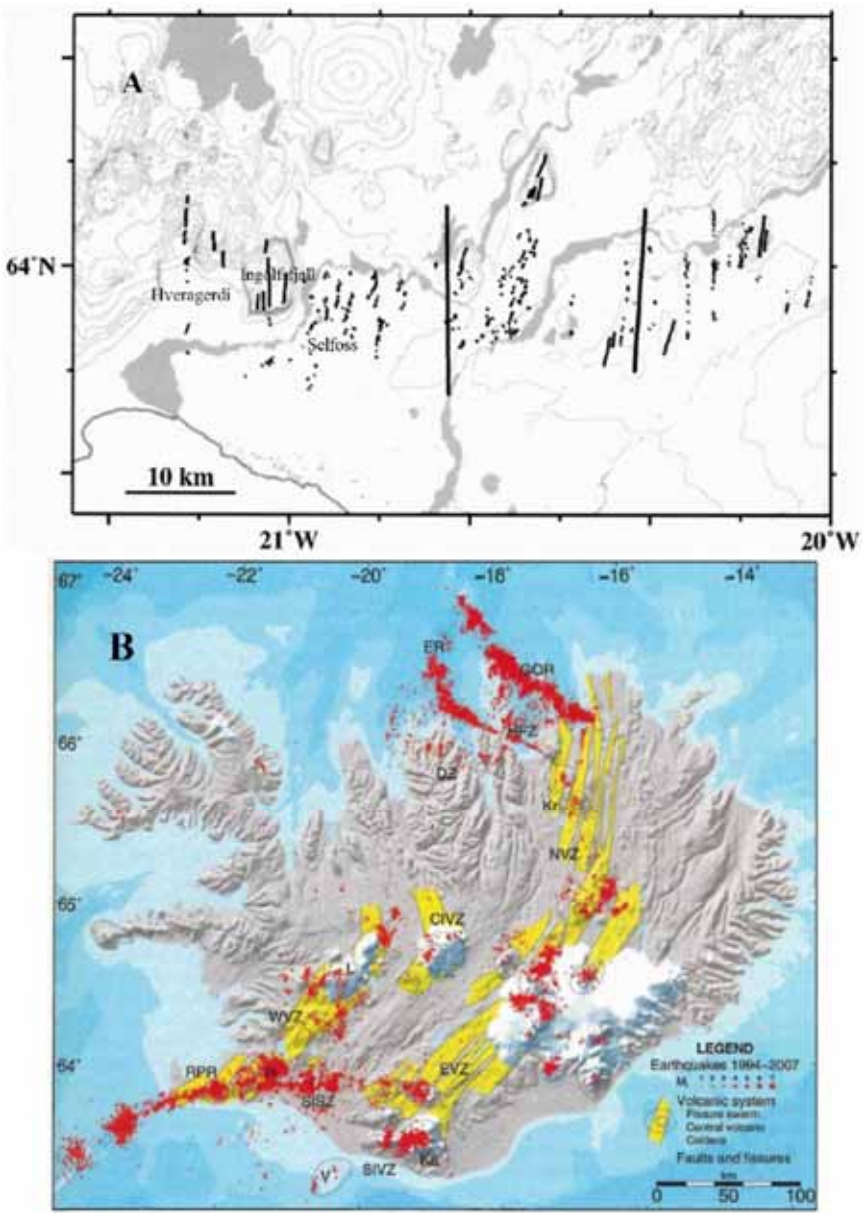

Figure 5: a) Mapped Holocene faults in South Iceland Seismic Zone; The heavy N-S lines show the source faults of the June 17 and 21, 2000 earthquakes; b) Red dots on the map shows earthquake epicenters 1994-2007 (Einarsson, 2008).

In the Grændalur central volcano, earthquakes with epicenters of magnitude less than 4 on the Richter scale are frequent. They were listed in 1991 and 1995 with significant seismic activity (Kyagulanyi D., 1996). Long before, other earthquakes with epicenters were recorded in 1915 or 1916 and in 1947, led to the remarkable change in surface hydrothermal activity (Saemundsson and Fridleifsson, 1992).

In June 2000, a series of earthquakes struck the South Iceland Seismic Zone (SISZ), two of which caused significant damage (Stefánsson et al., 2003). In the area, magnitude 6.5 activity began on June 17 in the eastern part and caused activity along the plate boundary of a stretch of about 90 km to the west as well as three other activities greater than magnitude 5 on the oblique rift of the Reykjanes Peninsula (Clifton et al., 2003; Pagli et al., 2003; Árnadóttir et al., 2004).

The recent earthquakes in the SISZ were produced on May 29, 2008. The location of the first earthquake of magnitude 5.5 was between the towns of Hveragerði and Selfoss and its epicenter was located at the south-western end of Mount Ingólfsfjall. Immediately after, the second earthquake of magnitude 6.3 occurred about 4 km west of the first earthquake and its epicenter was on an NS trending fault about 8 km WNW of Selfoss and 2 km in the SE of Hveragerði (Fig.6) (Icelandic Meteorological Office, 2008; Thorbjörnsson et al., 2009; Brandsdóttir, et al., 2010).

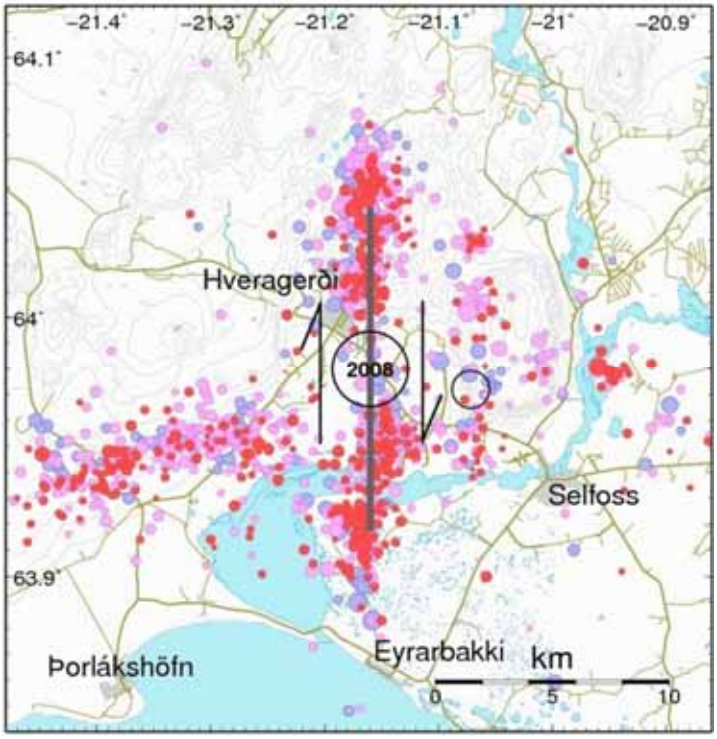

Figure 6: The epicenters of the earthquakes which occurred 29th May 2008; Rings represent the two major earthquake epicenters and small dots indicate minor earthquakes that occurred during the following three days (Icelandic Meteorological office, 2008).

2.3 Hveragerði geothermal field

The Hveragerði region is located on the eastern margin of the western rift zone mainly in the South Icelandic seismic zone (SISZ) (fig.7), in its western part which is in contact with the western flank of the active plate boundary between the North American and Eurasian crustal plates. It is part of three systems of the Hengill volcanic zone. These three systems are the Grændalur system, which is the oldest part, the Hrómundartindur system and the youngest being the Hengill system (Saemundsson, 1967; Ingólfsson et al., 2008).

The lithologic units of Hveragerði are mainly composed of hyaloclastites and intermediate basaltic lava units. All the rocks belonging to the Grændalur volcano are slightly inclined towards the west or north-west with a maximum inclination reaching up to 8°. In the region, faults are abundant and are often oriented NE-SW.

In the Hveragerði area, geothermal activity is still active mainly in the western and southern part. This geothermal activity is related to the NNE-SSW fractures or faults that strike the

region. The flow direction of the geothermal sources in this area is NE (fig.7). The location of the Hveragerði region in relation to Iceland's active volcanic belt and in conjunction with its drift out of this belt, the region is probably in the process of changing from a high-temperature geothermal system into a low-temperature system (Arnórsson, 1995a and b).

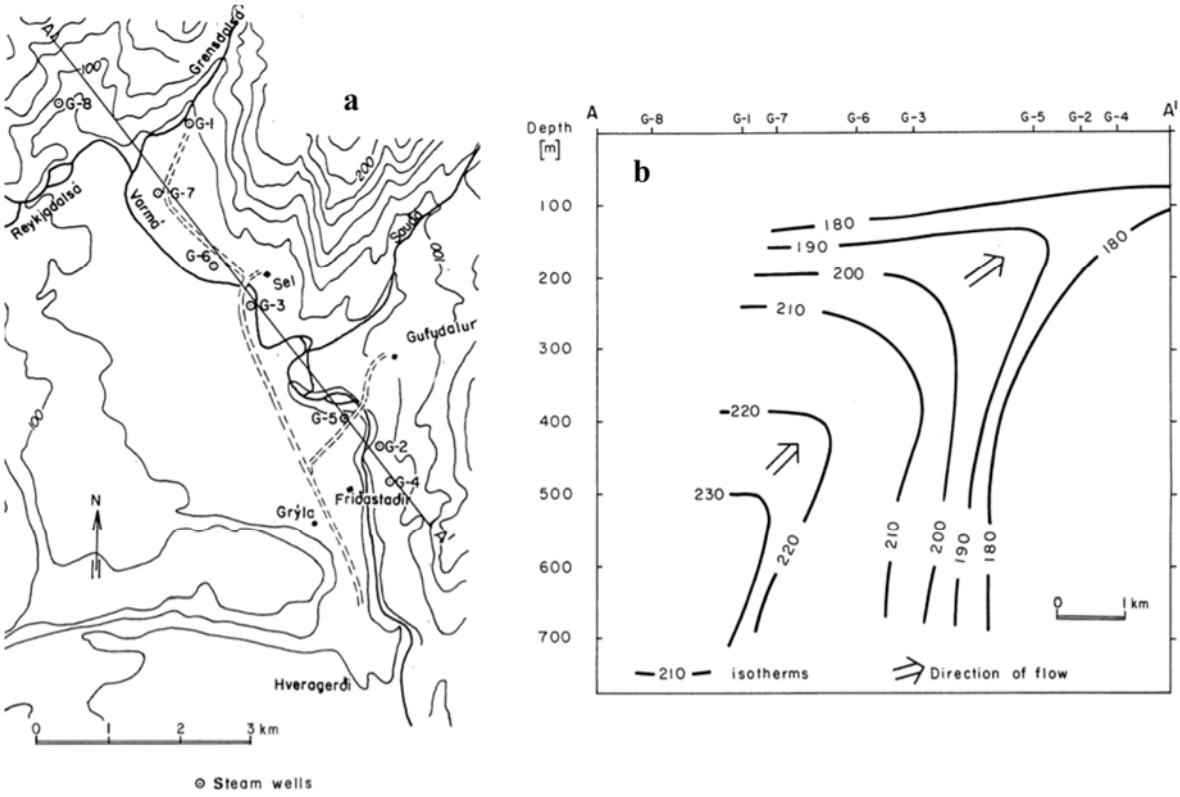

Figure 7: a: The high temperature geothermal field in Hveragerði; b: temperature distribution and geothermal flow direction in the cross-section of the figure a (Stefánsson V. and Steingrímsson B., 1980).

2.4 Geology of Grændalur area

The Grændalur area is mainly composed of basaltic rocks mainly tholeiite ranging from picrite to olivine and andesites as well as surface deposits. These basaltic rocks are subglacially hyaloclastites and interglacial lava flows. They are in particular vitreous tuffs, hyalocrystalline tuffs with porphyritic tuffs and rocks with aphyric, fine or coarse grain to variably porphyritic. Hyaloclastic and lava in Grændalur area are covered by superficial deposits (Saemundsson K. et al., 1994).

The lithostratigraphy of the Grændalur region from oldest to newest is presented as follows (fig.8):

- Formation of Varmár: is the oldest and most widely encountered rock group in the region. It is subdivided into three units:

  1. Breccias and pods of basalt lava form the core of the Varmár Formation. This formation is characterized by pods and blocks of basalt with a tuff matrix,

measuring tens of meters in width. These lava pods are dense, very fine-grained basalt without olivine of tholeiitic composition. They are elongated in an N-S direction.

2. Hyaloclastite tuff: it is a formation composed essentially of tuff or tuff-rich breccia which form thick units in inclined layers. It is a vesicular hyaloclastite with a relatively coarse texture without being brecciated.

In the Grændalur valley, heavily weathered glass is replaced by green chlorite and / or mixed layers of brown smectite.

It is in this formation that an important geothermal activity occurs due to the superficial nature of the rock faces and / or the deposit zones of the rivers (Saemundsson and Fridleifsson, 1992).

3. The lava flows.

- Tholeiitic lava: it is a formation of interglacial lava with fine grains and aphyric texture. They appear in the form of basalts articulated in irregular columns inclined 2-3° to the south.

- Kvíar basalt group: it is an interglacial formation which is essentially composed of lavas and breccias with a feldsparphyritic texture and often feldspar phenocrysts.

- Fluvial deposits: these are deposits that partly cover the Holocene lava flows in the plain in front of the valleys and others are found above some of the largest rock slides.

- Rock slides: they were certainly caused by large earthquakes linked to the SISZ. They are from the Holocene and cover much of the region.

Geological structures such as faults and fractures in the Grændalur region are mainly oriented NE-SW. But on the surface, these different structures are oriented NE-SW, NW-SE and N-S.

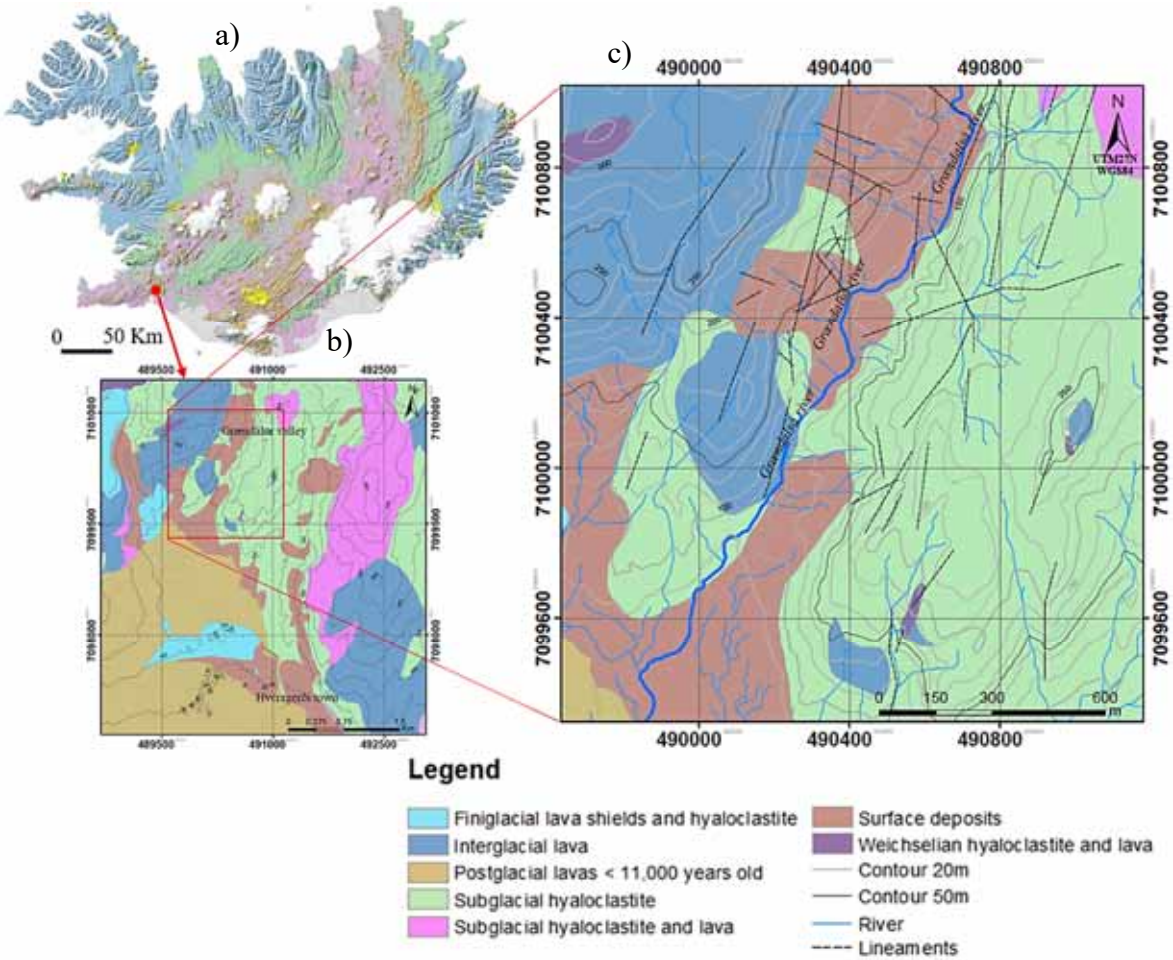

Figure 8: a: Map based on Geological map of Iceland. Iceland, 1:1.000.000 (Icelandic Institute of Natural History); b: Geological map of Hveragerði, c: Geological map of Grændalur valley (Saemundsson K. et al., 1994). Red circle and rectangle represent the approximate location of Grændalur valley.

3 Remote sensing and geothermal exploration

3.1 Overview of remote sensing

Remote sensing can be defined in general as the collection and interpretation of information about an object, area or event without being in physical contact with the object. Common platforms for remote sensing of the earth and its natural resources are aircraft/or drones and satellites (Sabins, 1999; Sanderson, 2014).

Remote sensing applies the techniques for taking images of the earth's surface in several wavelength regions of the Electromagnetic Spectrum (EMS). Some images are from solar radiation reflected in the visible and near infrared regions of the electromagnetic spectrum and others are measurements of the energy emitted by the earth's surface itself (In the region of the thermal infrared wavelength). The electromagnetic spectrum is the total range of wavelengths of electromagnetic waves emitted by matter whose temperature is above absolute zero (K) (Bakker H.W. et al., 2004). It is divided into seven regions which are gamma rays, X-rays, ultraviolet, visible light, infrared, microwaves, and radio waves (fig.9).

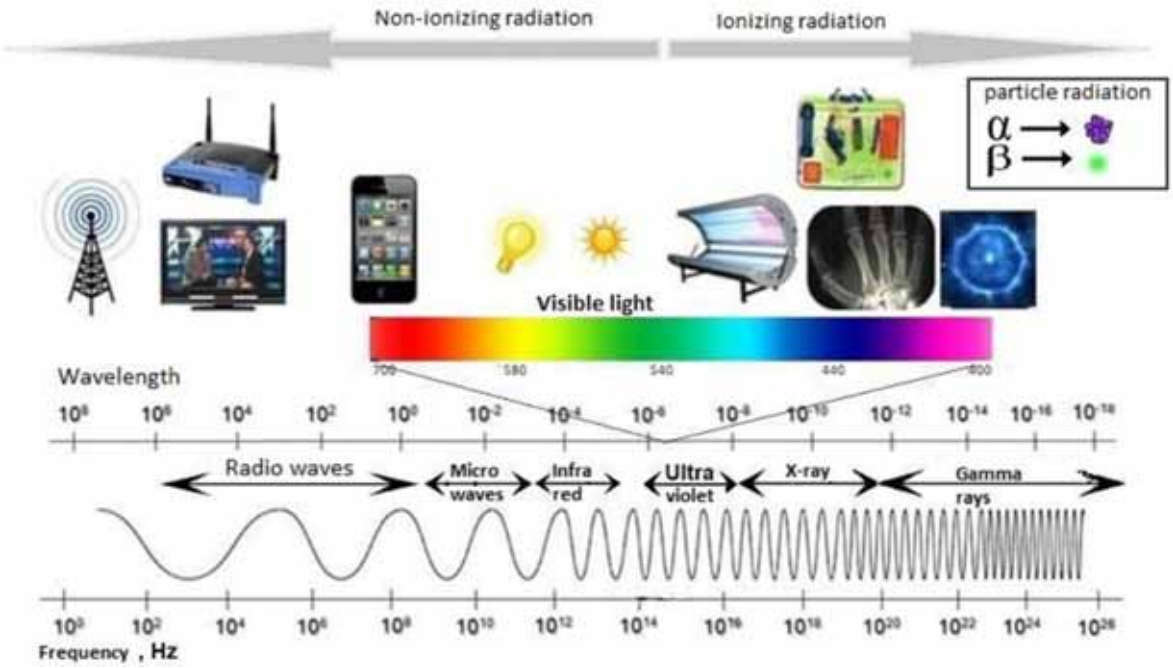

Figure 9: Seven regions of the Electromagnetic Spectrum (EMS) (From: www.uib.no).

In the microwave region, active remote sensing is called when the measured energy is the measure of the relative return of the earth's surface. It is an energy which is transmitted by the vehicle itself. Here, it is the remote sensing platform that provides the energy source. Conversely, when remote sensing measurements depend on an external energy source such as the sun, it is called passive remote sensing (fig.10).

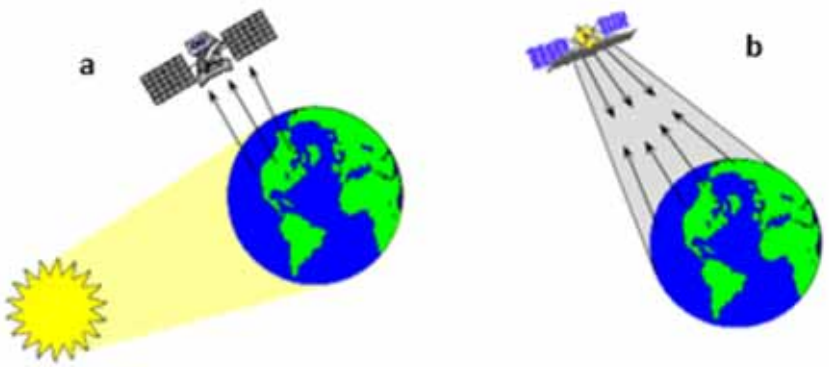

Figure 10: (a) Passive remote sensing, (b) Active remote sensing (Sanderson, 2014).

3.1.1 Principles of remote sensing

The detection of the object means the detection and recording of radiant energy reflected or emitted by that object. Generally, objects according to their properties (structural, physical and chemical) return a quantity of the energies in different bands of the electromagnetic spectrum incident on them.

The remote sensing process involves the following steps:

- Emission of electromagnetic radiation (EMR) (sun / self-emission)
- Transmission of energy from the source to the earth's surface, as well as absorption and scattering
- Interaction of emission of electromagnetic radiation (EMR) with the earth's surface: reflection and emission
- Transmission of energy from the surface to the remote sensor
- Sensor data output.

3.1.2 Electromagnetic radiation

The electromagnetic radiation is generally divided into two parts, there is the ionizing radiation which is a high frequency electromagnetic wave (above 10^{14} Hz) which has the ability to ionize the atomic bonds in cell molecules and the non-ionizing radiation which does not have enough energy (distributed in the range of 1 Hz to 10^{14} Hz) to separate the atomic bonds (photons) (Özkaya U. et al., 2018).

The modeling of electromagnetic energy (EM) can be done in two ways: by energy bearing particles called photons or by waves. In the wave model, the propagation in space at the speed of light c (approximately 299,790,000 m/s and can be rounded to 3.10^8 m/s) of electromagnetic energy is in the form of sine waves (Bakker H.W. et al., 2004). Generally, these waves are characterized by magnetic (M) and electric (E) fields. The two fields are perpendicular to each other and perpendicular to the direction of travel of the wave (fig.11).

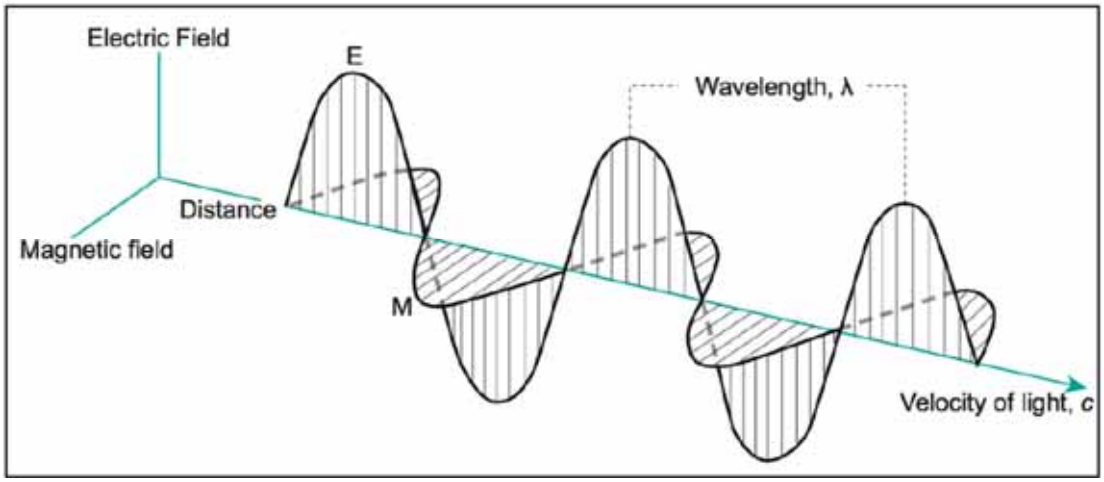

Figure 11: The EM radiation and its two components: Electric (E) and magnetic (M). From Bakker H.W. et al. (2004).

The speed of light being constant, the wavelength λ and the frequency v are inversely related to each other:

$$c = \lambda * v \qquad \textit{(Eq.1)}$$

The wavelength λ is defined as the distance between successive wave crests (fig. 11). It is measured in meters (m), nanometers (nm = 10^{-9} m) or micrometers (μm = 10^{-6} m). The frequency v is the number of cycles of a wave passing a fixed point over a specific period of time. It is measured in hertz (Hz) which is equivalent to one cycle per second.

3.1.3 Sources of electromagnetic energy (EM)

Due to the molecular agitation caused by the movement of molecules, any matter with a temperature above zero emits electromagnetic energy. That is, the sun and the earth radiate energy in wave forms. Any matter capable of absorbing and re-emitting the electromagnetic energy it receives is called a blackbody. Here, absorbance and emissivity (the emission capacity of a real material compared to that of the black body) are equal to 1. These two parameters have a huge influence on the amount of energy radiated by an object, which is a function of the wavelength. Stefan-Boltzmann's law defines this principle by saying that a black body radiates a continuum of wavelengths (Bakker H.W. et al., 2004) (fig.12).

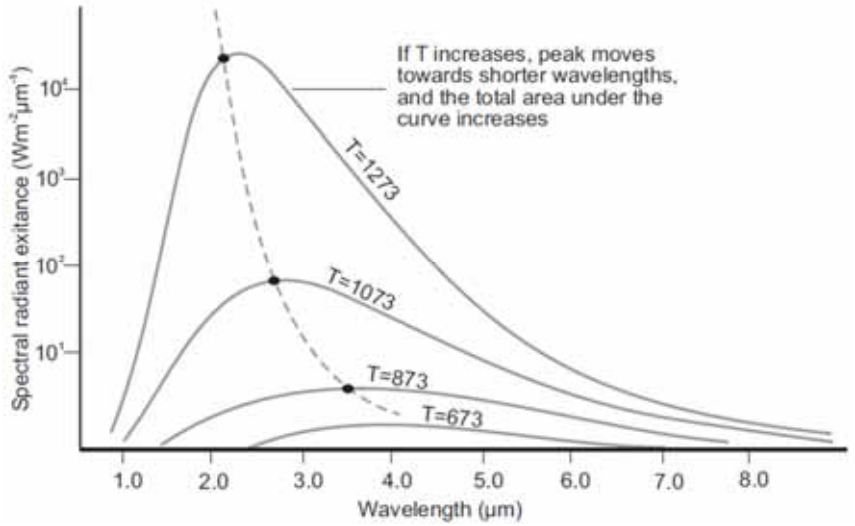

Figure 12: Blackbody radiation curves based on Stefan-Boltzmann's law (with temperatures T, in K). The radiation peak at 400°C (673 K) is about 4 µm while the radiation peak at 1000°C is 2.5 µm. The higher temperature corresponds to a greater contribution of shorter wavelengths (from Bakker H.W. et al., 2004).

3.1.4 Electromagnetic energy (EM) interactions with the Earth's surface

When solar radiation is incident on the earth's surface, it is either transmitted to the surface, reflected by the surface, or absorbed and emitted by the surface (Fig.13). During the interaction, electromagnetic energy undergoes changes in direction, amplitude, polarization, phase and wavelength. These different changes are detected by the remote sensor. The information collected can be either spatial data related to size, shape and orientation or spectral data related to tone, color and spectral signature (Bakker H.W. et al., 2004).

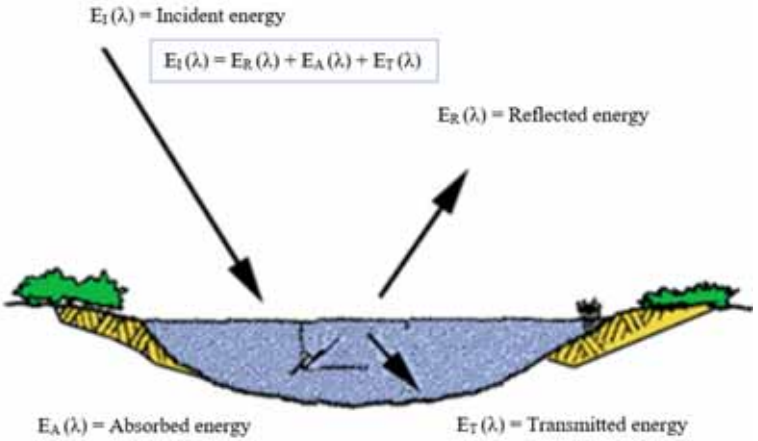

(Eq.2)

Figure 13: Electromagnetic energy interactions with the Earth's surface (from http://gsp.humboldt.edu/).

a. Reflection

It is a phenomenon that occurs when a ray of light is redirected when it bounces a non-transparent surface (fig.14).

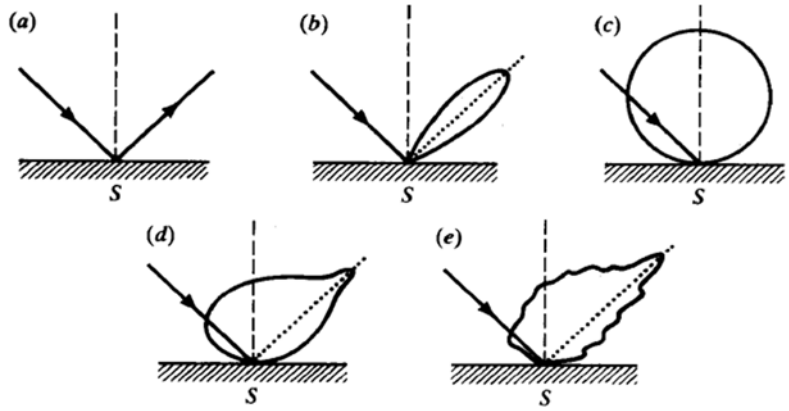

Figure 14: Types of scattering surfaces (a) Perfect specular reflector (b) Near perfect specular reflector (c) Lambertain (d) Quasi-Lambertian (e) Complex (from Bakker H.W. et al., 2004).

b. Transmission

Radiation transmission is the phenomenon that occurs when radiation passes through a substance without significant attenuation (fig.15). The transmittance (τ) which is the capacity of a medium to transmit energy is calculated by:

$$\tau = \frac{\text{Transmitted radiation}}{\text{Incident radiation}} \qquad \textit{(Eq.3)}$$

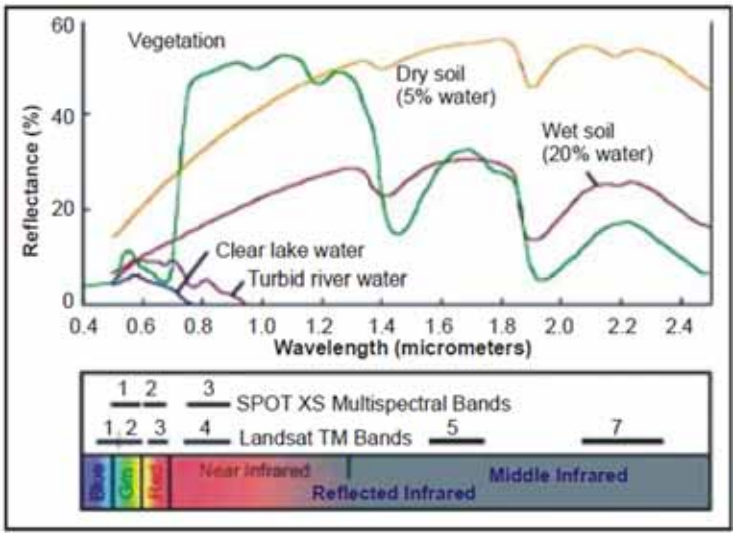

Figure 15: Typical Spectral Reflectance curves for vegetation, soil, and water. From Jiang C.Y.H., 2013)

3.1.5 Electromagnetic energy (EM) interactions with the atmosphere

As the sun is the most important source of energy, it encounters three interactions in the atmosphere before it reaches the earth's surface (Bakker H.W. et al., 2004). These interactions are either absorption, transmission, or scattering. The surface material reflects or absorbs the energy transmitted by the sun (fig.16).

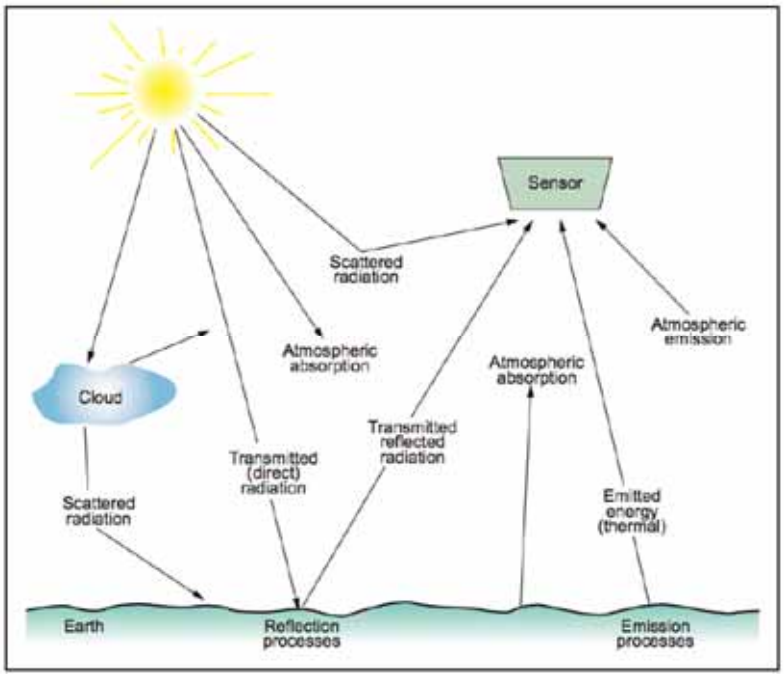

Figure 16: Electromagnetic energy interactions with the atmosphere and the earth's surface. From Bakx et al., (2012).

a. Absorption and transmission

Some of the electromagnetic energy that passes through the atmosphere can be absorbed either by ozone (O_3), water vapor (H_2O) and carbon dioxide (CO_2). Remote sensing can only use wavelength regions outside the main absorption bands of atmospheric gases. These regions are called atmospheric transmission windows. Because outside of these areas, no corresponding energy can enter the atmosphere. Typically, optical remote sensors operate in windows between 0.30 and 14 μm (fig.17).

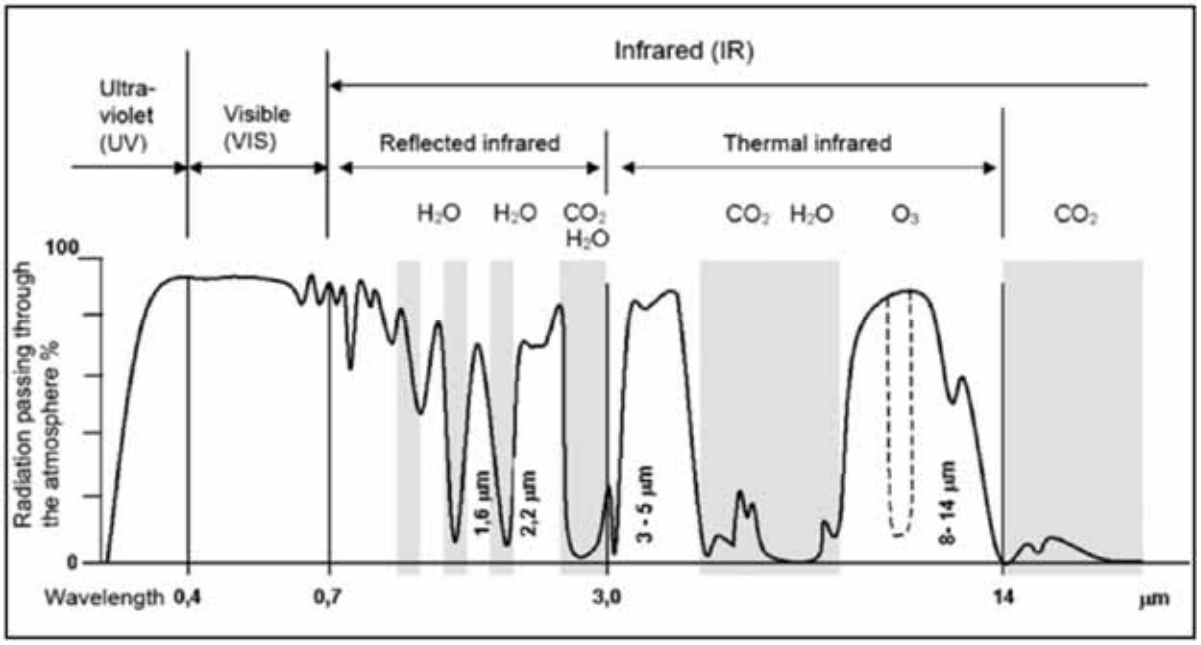

Figure 17: Atmospheric transmission

b. Atmospheric scattering

It is a phenomenon which occurs in the atmosphere when the gaseous particles and molecules manage to cause the reorientation of the original path of electromagnetic waves. Several factors contribute to the amount of scattering, including the wavelength of the radiation, the amount of particles and gases and the distance traveled by the radiation through the atmosphere (Bakker H.W. et al., 2004).

3.1.6 Thermal remote sensing

All objects with a temperature above absolute zero (0 K, which equals -273°C) emit electromagnetic radiation. The earth has an average temperature of about 300 K and its peak of electromagnetic emittance is located in the thermal infrared (TIR) of the electromagnetic spectrum (EMS), domain at about 9.7μm (Kuenzer and Dech, 2013). Thermal remote sensing is based on the measuring of electromagnetic radiation (EM) in the infrared region of the spectrum. Most commonly used are the intervals from 3–5 μm (MIR) and 8–14 μm (TIR), in which the atmosphere is fairly transparent, and the signal is only lightly attenuated by atmospheric absorption (Bakker H.W. et al., 2004).

The most important property in thermal remote sensing is the quality of emitted energy from the surface at different wavelengths. Not dependent on the incoming sun, thermal remote sensing can also be performed during the night. The amount of energy emitted per wavelength as a function of the temperature of objects is described by Planck's blackbody radiation law:

$$M_{\lambda,T} = \frac{2\pi hc^2}{\lambda^5 \left(e^{hc/\lambda kT} - 1\right)} \qquad \textit{(Eq.4)}$$

where,

- $M_{\lambda,T}$ is the spectral radiant emittance in (W m^{-2} μm^{-1}), it can be calculated from the body's temperature (fig.18)
- λ is the wavelength in (μm)
- h is Planck's constant (6.626 x 10^{-34} J s)
- c is speed of light (2.9979246 x 10^{8} m s^{-1})
- k is Boltzmann constant (1.3806 x 10^{-23} j K^{-1})
- T is the absolute temperature in (K)

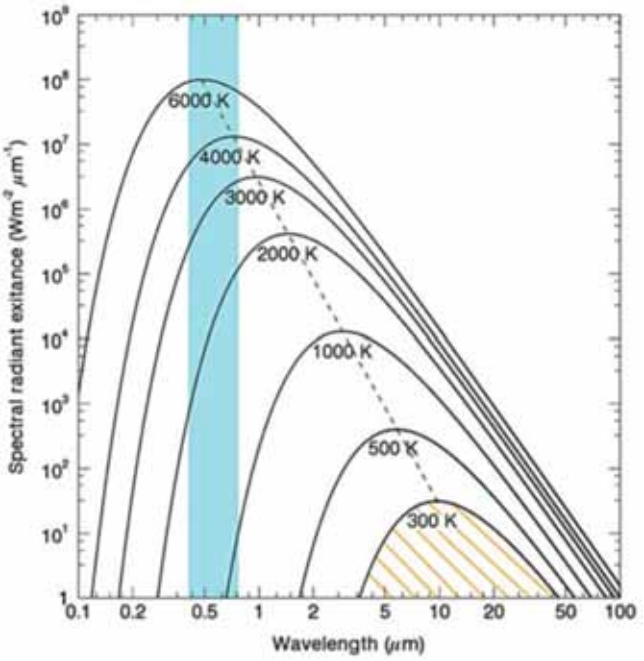

Figure 18: Blackbody radiation curves as a function of temperature, derived from Eq. 4. The area under the 300 K curve represents the Planck, Stefan-Boltzmann laws, the green dashed line represents Wien's law, and the blue bar indicates the visible radiation energy band (Kuenzer and Dech, 2013).

The total electromagnetic radiation emitted by a blackbody as a function of the absolute temperature of that body is described by the Stefan-Boltzmann law (Kuenzer and Dech, 2013):

$$T_{RadBB} = \sigma T_{kin}^{4} \qquad \textit{(Eq.5)}$$

where:

- T_{RadBB} is radiant flux of a blackbody (W/m^2)
- T is absolute kinetic temperature (K)
- σ is Stefan-Boltzmann constant (5.6697×10^{-8} W m^{-2} K^{-4})

The wavelength at which maximum spectral radiant exitance occurs is described by the Wien's law (Bakker H.W. et al., 2004):

$$\lambda_{max} = \frac{A}{T} \qquad \textit{(Eq.6)}$$

where,

- λ_{max} is wavelength of maximum spectral radiant exitance (μm)
- A is Wien's constant (2897.8 μm K)

- T is absolute kinetic temperature (K)

From the kinetic temperature, most objects emit less radiation and do not act like perfect black bodies. This fact is taken into account by the emissivity coefficient (ε (λ)). ε is the radiant flux of an object at a given temperature over the radiant flux of a blackbody at the same temperature. All the radiation absorbed by a black body is emitted again. According to Kirchhoff's law (1860), the emittance at a given wavelength is equal to its absorbance at the same wavelength (Kuenzer and Dech, 2013):

$$\varepsilon_{(\lambda)} = \alpha_{(\lambda)} \qquad \textit{(Eq.7)}$$

Taking into account energy conservation, where the sum of absorption (α), reflection (ρ), and transmission (τ) equals 1, and Eq. 7:

$$\varepsilon_{(\lambda)} + \rho_{(\lambda)} + \tau_{(\lambda)} = 1 \qquad \textit{(Eq.8)}$$

As most objects are opaque and do not transmit radiation, Eq. 8 can be re-formulated as:

$$\varepsilon(\lambda) + \rho(\lambda) = 1 \qquad \textit{(Eq.9)}$$

Generally, emissivity does not depend on the temperature, it varies according to the type of surface and the wavelength. Based on Eq. 5 and the definition of emissivity, the conversion of the radiation temperature into kinetic temperature is done by:

$$T_{(rad)} = \varepsilon^{(1/4)} * T_{(kin)} \qquad \textit{(Eq.10)}$$

For real materials, the emissivity is below 1 and the radiance temperature $T_{(rad)}$ measured by a sensor is always lower than the real kinetic (surface) temperature, $T_{(kin)}$, of an object (fig.19).

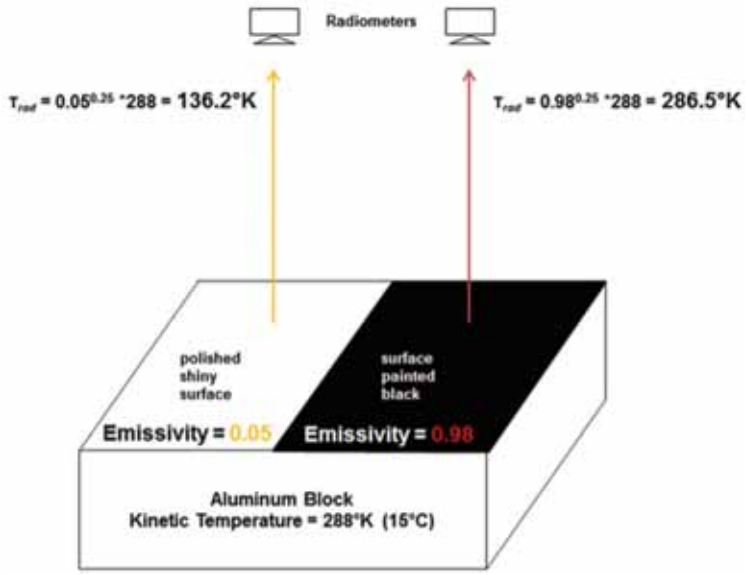

Figure 19: Impact of emissivity on radiance temperature recorded at the sensor (Kuenzer and Dech, 2013).

3.2 Remote sensing applied to geothermal exploration

The word geothermal originates from two Greek words, “geo”, meaning earth, and “thermos”, meaning heat since it is the energy extracted from heat stored in the earth. This energy, which comes from the radioactive decay of minerals and solar energy absorbed at the surface, leading to the formation of magma whose temperature of can reach around 5500°C (Mburu M., 2014). Typically, the temperature gradient is around 15° to 30°C per kilometer in the crust but can be as high as 150°C per kilometer in hot geothermal areas (Saemundsson K., 2009).

Geothermal systems are classified in various ways based on heat source, heat transfer, reservoir temperature, physical state, use, and ecological parameters. The common classification of geothermal systems is (Saemundsson K., and al., 2009):

(a) volcanic systems with hot intrusions or magma chambers in the crust as the heat source,

(b) convective systems with deep water circulation in tectonically active zones of high geothermal gradient,

(c) conductive sedimentary systems with permeable layers at great depth (2-5 km),

(d) geopressured systems often in conjunction with petroleum resources,

(e) hot dry rocks or EGS systems where anomalously hot masses of low permeability rocks occur at drilling depths,

(f) shallow resources in normal geothermal gradient zones used with geothermal heat pump applications.

Water is the main heat carrier for extracting energy from the underground. Surface water eventually rainwater passes through existing fractures in the crust to reach the subsurface and exchange heat with the rocks. In the crust, two forms of heat transfer generally occur: conduction and convection (fig.20).

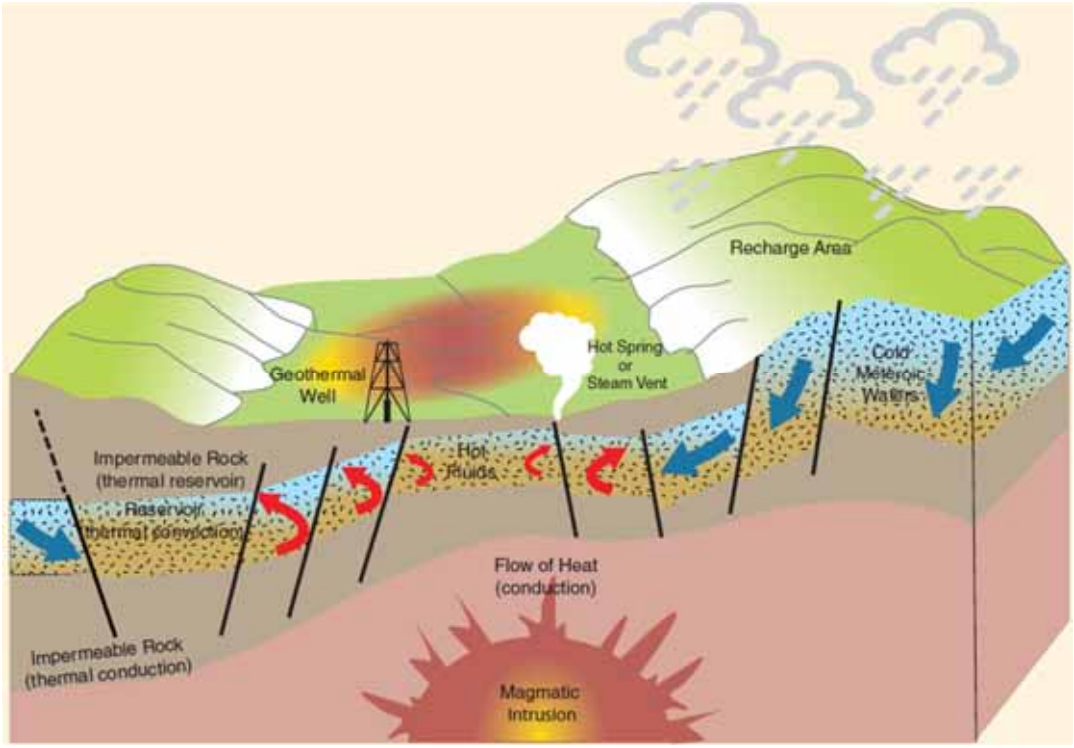

Figure 20: The components of a typical hydrothermal (steam or water based) volcanic-related geothermal system (Source: Gehringer and Loksha, Geothermal Handbook: Planning and Financing Power Generation, ESMAP, 2012).

In the convective system, aquifers represent the geothermal reservoir. It is a hydrothermal resource. It is a system found in areas where the rocks are very fractured and the circulating fluids are abundant, the heat transfer under these conditions is very efficient and can be easily exploited by drilling wells to evacuate the hot fluids to the surface over a range of temperature and discharge rate (Manzella A., 2017). They are used to generate electrical energy or other uses (Table 1). These hot fluids can be returned to the surface following fractures and lead to the formation of surface geothermal manifestations such as the hot ground, boiling springs, geysers, hot springs, mud pots, hydrothermal alteration, fumaroles, and steam vents (Heasler et al., 2009) (fig.21). These geothermal manifestations provide important information for geothermal site selection, exploration and even production. They are also the subject of geothermal remote sensing studies.

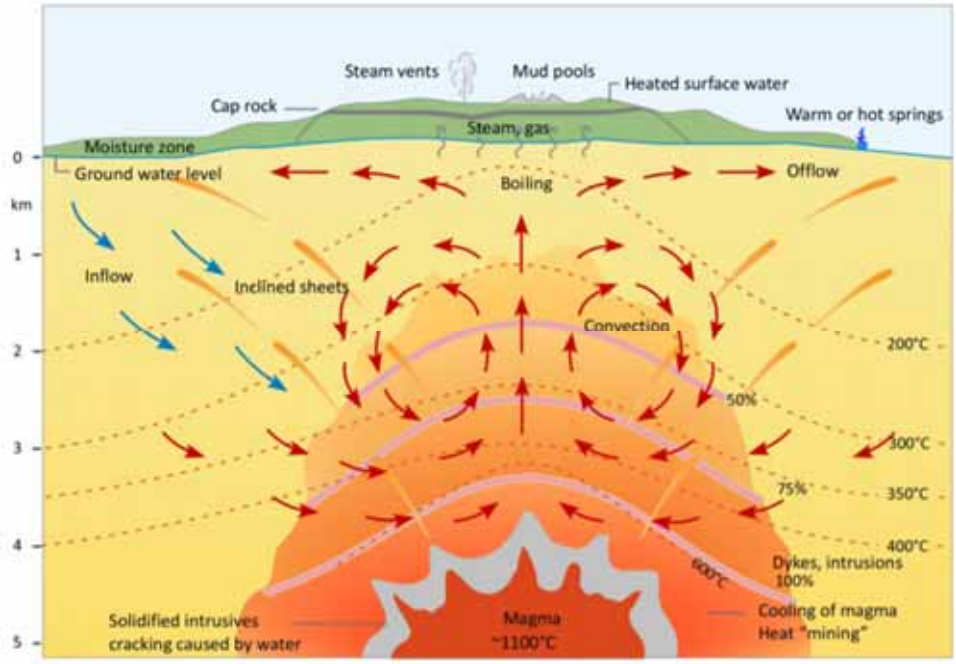

Figure 21: Simplified model of a high temperature geothermal system (Saemundsson K., 2009).

Table 1: Basic technology commonly used for geothermal energy (Mburu M., 2014)

Reservoir temperature	Reservoir fluid	Common use	Technology commonly chosen
High temperature, >220°C	Water or Steam	Power generation Direct use	Flash steam; Combined (flash and binary) Direct fluid use; Heat exchangers; Heat pumps
Intermediate temperature, 100-220°C	Water	Power generation Direct use	Binary cycle Direct fluid use; Heat exchangers; Heat pumps
Low temperature, 30-150°C	Water	Direct use	Direct fluid use; Heat exchangers; Heat pumps

In geothermal development project, one of the most important phases is exploration. It is a phase that involves several methods. This phase aims to define the geometry and characteristics of the geothermal system. The methods are frequently involved are:

- ***Geology:*** This method invariably starts at the incipient reconnaissance stage, which entails preliminary mapping (photogeology and remote sensing) of the lithologic units and structures, geo-hazards, environmental geology, mapping of thermal surface manifestations and possibly relate to the structures and or volcanism of region. Detailed geological studies are performed in the geothermal field and its surroundings (Árnason K. and Gíslason G., 2009). In this part, it's important to mapping rock units, intrusions types and their chronological sequence (lithological mapping) in order to understand the volcanological evolution and the stratigraphy. Performed the mapping of

geothermal alteration on the surface and analyzed the alteration minerals in order to understand the temporal variation in the surface activity. An exhaustive mapping of thermal manifestations is performed, and the physical properties of surface manifestations are measured and recorded, including temperature, flow rate, conductivity etc. (Árnason and Gíslason, 2009). Petrological and petrochemical rock analysis in the surface and in depth (cuttings analysis) is performed to be able to distinctively understand the rocks units starting from the surface to depth taking into account alteration minerals. Structural mapping is done in the effort to distinguish the main types of faults and fissures that transect the geothermal prospect of interest and be able to discern the structural controls of the system (Leakey O., 2013). Propose a conceptual model of the region that will be updated after each stage of exploration.

- ***Geochemistry***: The geochemical methods in geothermal exploration consist of the sampling, analysis and interpretation of discharge of thermal fluids from fumaroles, hot springs and steaming grounds. The main objectives of geochemical studies are to characterize the thermal fluids, establish their origin, flow direction (upflow and outflow), evaluate mixing scenarios, estimate the equilibrium reservoir temperature (geothermometry) (rock forming constituents: SiO_2, Na, K, Ca, Mg, CO_2, H_2,..) and to determine the suitability of the fluids for the intended use (Leakey O., 2013). The analysis of rock forming constituents allows to predict subsurface temperatures and potential production problems such as deposition and corrosion (Ármannsson and Fridriksson, 2009). In the surface, the diffuse soil degassing measurements of CO_2, ^{222}Rn, ^{220}Rn, and Hg and Hg is essential in delineating permeable zones (gas leakages) of the system associated with fractures, fissures, and other geological structures (Fridriksson, 2009).

- ***Geophysics***: In geothermal exploration, geophysical methods basically aim at determining geometry (shape, size, depth) of the heat source, reservoir, cap rock. Additionally, the methods aim at imaging structures that are responsible for the geothermal system, fluid pathways, stress field and delineating the areal extent of the geothermal resource. The most commonly used geophysical methods are electromagnetic/electric, gravity, magnetics and seismics. These methods ultimately depend on the various intrinsic properties of rocks such as resistivity/electrical conductivity, density, magnetic susceptibility, elastic moduli/velocity respectively. Geothermal anomalies are linked to geophysical anomalies because changes in temperature and geothermal gradient can change subsurface physical properties that influence measurements at the surface (Pipan, 2009). In this respect, a geothermal system generally causes inhomogeneities in the physical properties of the subsurface, which can be observed to varying degrees as anomalies measurable from the surface. The changing physical properties can be measured using different geophysical methods and instruments (Table 2).

Table 2: Physical properties and the corresponding geophysical methods and instrument (Leakey O., 2013)

Physical property	Geophysical method	Common equipment
Electrical conductivity/resistivity	Electromagnetic/electric	MT/TEM
Density	Gravity	Gravimeter
Magnetic susceptibility	Magnetics	Magnetometer
Elastic Moduli/velocity	Seismic	Seismometer

- ***Drilling:*** the drilling test which is the first full diameter exploration well to confirm the presence of the resource is drilled if the results of the previous methods are promising. This is a time of the highest risk (Harvey C. and al., 2013).

Geothermal remote sensing can be linked to geological method during geothermal exploration. It has a synoptic ability to cover large areas in real time and can quickly explore potential geothermal sites that are difficult to detect and access using conventional survey methods.

Van der Meer et al., (2014) subdivide the surface anomalies that can be detected from remote sensing into two groups:

- Direct evidence of geothermal activity that can be extracted by remote sensing is found in anomalous mineral assemblages and surface features such as geothermal manifestations and geological structures (faults, fractures and lineaments).

- Indirect evidence which is usually surface temperature variations related to the presence of heat sources that can be measured and mapped using thermal infrared radiation.

In geothermal exploration, remote sensing can contribute to the mapping of (Van der Meer et al., 2014):

- surface deformation and heat flow measurements: using interferometric SAR (Synthetic Aperture Radar) to monitor subsidence and surface deformation at geothermal sites.

- Temperature: It consists of mapping the surface temperature and correlating it to geothermal heat using TIR (thermal infrared) data from daytime and night-time ASTER images, or combined ASTER and MODIS acquisitions, or Landsat 7 Enhanced Thematic Mapper + (ETM +), or Landsat 8 Operational Land Imager (OLI), etc. This part is the subject of our study and will be developed below.

- geobotany: the identification of vegetation species diversity in geothermal areas can be done by multi and hyperspectral optical remote sensing.

- structural analysis: allowing to reconcile stratigraphy, hydrogeology and structural geology to better understand the circulation of the geothermal fluid in the reservoir. It

is done by combining multispectral enhanced images and products derived from digital terrain models derived from either SAR or LIDAR datasets or using SRTM DEM/Artic DEM image.

- gas emissions: quantifying gaseous emissions from geothermally active areas by combining multispectral (Airborne TM and CASI, the compact Canadian hyperspectral instrument Airborne Spectrographic Imager), hyperspectral (Specim Eagle) and LIDAR (light detection and ranging) data.

- surface alteration minerals: It is done by identifying surface alteration minerals from the multispectral and hyperspectral datasets of ASTER images or combining them with other types of images such as MODIS, MASTER, SEBASS (Spatially Enhanced Broadband Array Spectrograph System; a hyperspectral thermal instrument), HyMAP (the Hyperspectral Mapper airborne hyperspectral), AVIRIS (the Airborne Visible / Infrared Imaging Spectrometer), etc.

In geothermal exploration, the choice of sensors (aircraft, drones or satellites) depends on the research objective. For the efficiency of the results, several sensors can be used to compare or complement the results obtained. Because each sensor has its own acquisition mode and spatial and spectral resolution.

In general, this remote sensing is one of the fastest mapping methods and is applied to geothermal exploration to study surface geothermal manifestations by quantifying thermal anomalies associated with surface geothermal features such as fumaroles, hot springs, etc., and to evaluate new resources (Mongillo, 1994; Allis et al, 1999; Eneva et al, 2006; Kratt et al, 2006; Kratt et al, 2006; Eneva et al, 2007; Rockwell and Hofstra, 2008; Kienholz et al, 2009; Littlefield and Calvin, 2009; Scherer et al, 2009; Taranik et al, 2009; Littlefield and Calvin, 2010; Haselwimmer et al, 2011).

TIR sensors are used to derive thermal radiation images of objects on the earth's surface. The radiance images derived can display the kinetic temperature of objects at the resolution of the respective sensor (Kuenzer and Dech, 2013). One of the best-known products derived from TIR imagery is the Earth's surface temperature (Dech et al. 1998). Data from TIR sensors allow the evaluation of thermal anomalies. These data can be acquired during the daytime or nighttime independent of the sun as an illumination source. Nighttime data is especially suitable for detecting thermal anomalies, such as weak thermal anomalies induced by geothermal phenomena. During the day, uneven solar heating due to the varying sun-sensor-object geometry, topography and thermal inertia can hinder the extraction of thermally anomalous pixels (Kuenzer and Dech, 2013).

4 Data and methods

4.1 Geothermal mapping in Grændalur

The geothermal mapping takes into account the spatial representation of different types of geothermal manifestations that occur in the study area. To do this, the description of the geothermal manifestation was made in situ, the manifestations temperature measurements were performed using a digital thermometer and the positioning of their sampling points was done by GPS. After field work, the collected data were downloaded to a computer and edited by ArcGIS 10.6 software (fig.22). The digital elevation model (DEM) *'IslandsDEMv0_2x2m_zmasl_isn2016_58'* downloaded from the website www.lmi.is, was used to determine the geological structures of the area. The result is a geothermal map on a scale of 1: 8000 showing the geothermal manifestations and tectonic structures distribution in the Grændalur valley.

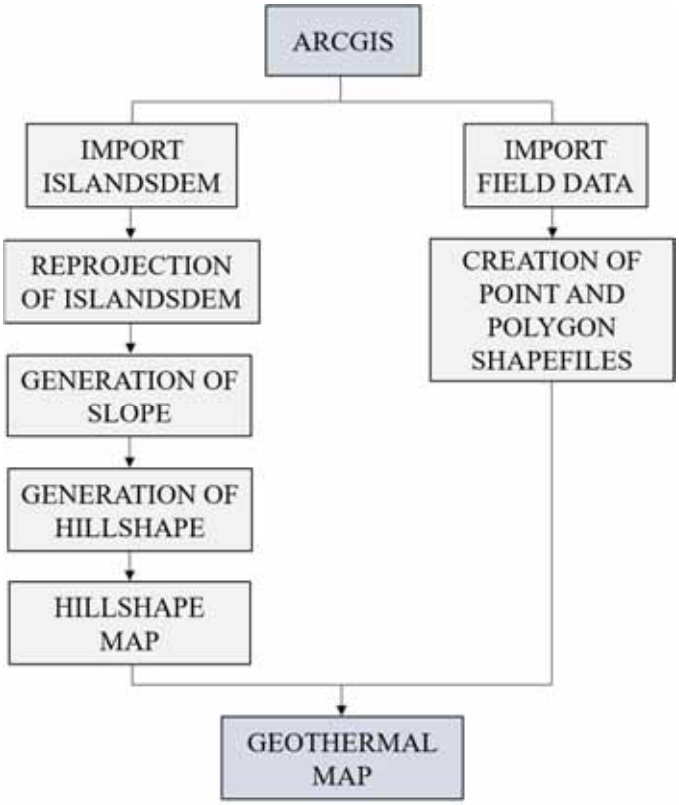

Figure 22: Steps followed for the geothermal mapping.

4.2 Identification of thermal anomalies

4.2.1 Satellite based LST retrieval

The identification of thermal anomalies was made using Landsat and ASTER images. These images were downloaded from the USA Geological Survey (USGS) Earth Explorer web page. Their processing levels were L1 TP for Landsat and L1T for ASTER. Standard data for these levels is a radiometrically calibrated sensor, with systematic geometric corrections applied using spacecraft and DEM ephemeris data to correct for relief displacement and rotated to a Northup UTM projection. The scenes (daytime and nighttime) are provided in GeoTIFF format. The images used and their spectral and spatial resolution are shown in Tables 3 and 4. The collected data were downloaded to a computer and edited by ArcGIS 10.6, ENVI 5.3 and QGIS 3.16 software.

Table 3: List of satellite image data sets downloaded from the USGS Earth Explorer webpage.

Platform - Satellite	Acquisition date	Code
Landsat 7 ETM+	May 13th, 2007 (Daytime scene)	b
	July 16th, 2008 (Daytime scene)	c
Landsat 8 OLI & TIRS	April 23th, 2015 (Nighttime scene)	f
	August 31st, 2016 (Nighttime scene)	g
	October 21st, 2017 (Nighttime scene)	h
	October 24th, 2018 (Nighttime scene)	i
	May 04th, 2019 (Nighttime scene)	j
	November 14th, 2020 (Nighttime scene)	k
Terra - ASTER	December 15th, 2005 (Nighttime scene)	a
	February 25th, 2009 (Nighttime scene)	d
	May 20th, 2011 (Daytime scene)	e

Table 4: Spectral coverage and spatial resolution from the satellite data used; (*) indicates resampled.

Platform - Satellite	Band number	Wavelength (µm)	Spatial resolution (m)
Landsat 7 ETM+	1: Blue	0.45-0.52	30
	2: Green	0.52-0.60	30
	3: Red	0.63-0.69	30
	4: Near infrared (NIR)	0.77-0.90	30
	5: Shortwave infrared (SWIR-1)	1.55-1.75	30
	6: Thermal infrared (TIR)	10.40-12.50	60*(30)
	7: Shortwave infrared (SWIR-1)	2.09-2.35	30
	8: Panchromatic	0.52-0.90	15
Landsat 8 OLI & TIRS	1: Ultra-Blue (coastal/aerosol)	0.435-0.451	30
	2: Blue	0.452-0.512	30
	3: Green	0.533-0.590	30
	4: Red	0.636-0.673	30
	5: Near infrared (NIR)	0.851-0.879	30
	6: Shortwave infrared (SWIR-1)	1.566-1.651	30
	7: Shortwave infrared (SWIR-2)	2.107-2.294	30
	8: Panchromatic	0.503-0.676	155
	9: Cirrus	1.363-1.384	30
	10: Thermal infrared (TIRS-1)	10.60-11.19	100*(30)
	11: Thermal infrared (TIRS-2)	11.50-12.51	100*(30)
Terra - ASTER	1: Visible and near infrared (VNIR)	0.52-0.60	15
	2: Visible and near infrared (VNIR)	0.63-0.69	15
	3: Visible and near infrared (VNIR)	0.76-0.86	15
	4: Shortwave infrared (SWIR)	1.60-1.70	30
	5: Shortwave infrared (SWIR)	2.145-2.185	30
	6: Shortwave infrared (SWIR)	2.185-2.225	30
	7: Shortwave infrared (SWIR)	2.235-2.285	30
	8: Shortwave infrared (SWIR)	2.295-2.365	30
	9: Shortwave infrared (SWIR)	2.360-2.430	30
	10: Thermal infrared (TIR)	8.125-8.475	90
	11: Thermal infrared (TIR)	8.475-8.825	90
	12: Thermal infrared (TIR)	8.925-9.275	90
	13: Thermal infrared (TIR)	10.25-10.95	90
	14: Thermal infrared (TIR)	10.95-11.65	90

The processing of the data for thermal anomaly mapping used in this study was done according to the procedure presented in figure 23.

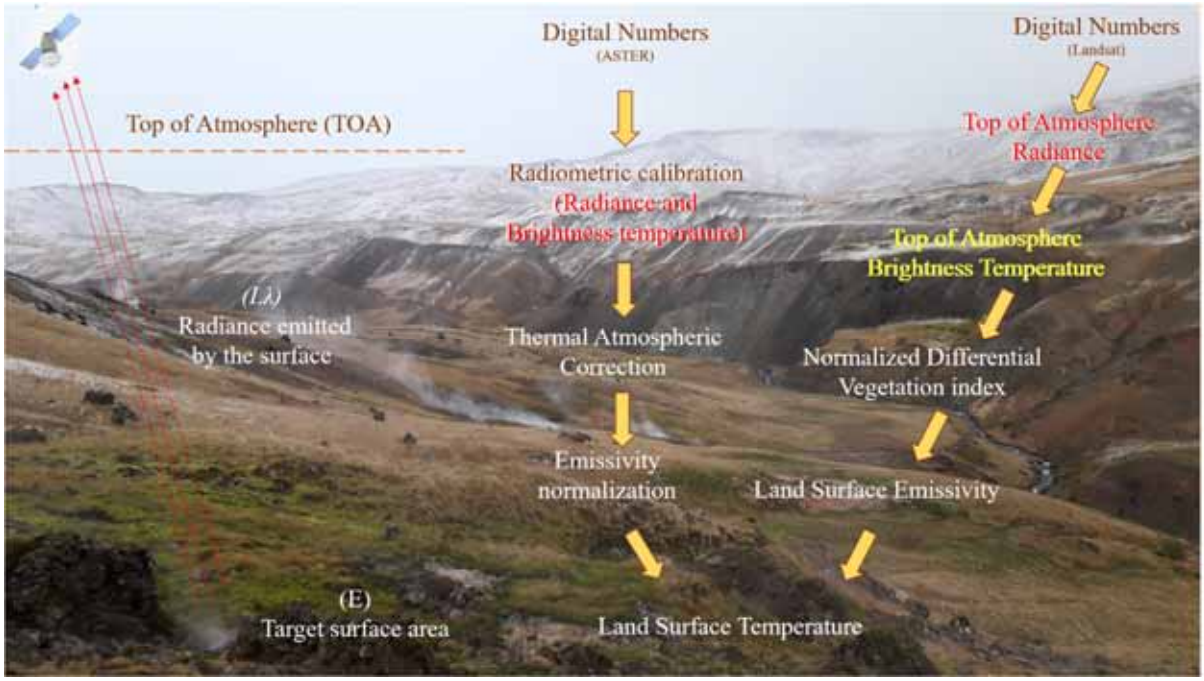

Figure 23: Data processing steps followed for thermal anomaly mapping retrieved by the satellite.

The estimation of LST values with Landsat is done using the thermal band 6 (Landsat 7) and band 10 (Landsat 8) according to the steps:

1. Top of atmosphere (TOA) radiance

Radiance includes the radiation reflected from the surface, in addition to the radiation that bounces in from neighboring pixels. The values in the selected band were converted to spectral radiance at the top of the atmosphere (TOA) ($L\lambda$) using the formula below:

$$L\lambda = M_L * Qcal + A_L \qquad (Eq.11)$$

where,

- $L\lambda$ is Spectral radiance ($W/(m^2 * sr * \mu m)$)
- M_L = Radiance multiplicative scaling factor for the selected band taken from the metadata of the image
- A_L = Radiance additive scaling factor for the selected band from the metadata
- Qcal is the level 1 pixel value of selected band.

2. Top of atmosphere (TOA) Brightness Temperature

Brightness temperature is the temperature of a blackbody that would emit the same amount of radiation as the targeted body in a specified spectral band. The spectral radiance then converted to brightness temperature at the sensor (BT) with the following formula (U.S. Geological Survey, 2016):

$$BT = \frac{K_2}{\ln(K_1/L\lambda + 1)} - 273.15 \qquad (Eq.12)$$

where:

- BT is the TOA brightness temperature (◦C),
- $L\lambda$ is TOA spectral radiance,
- K_1 = Band 10 thermal conversion constant from the metadata (Landsat 8) or 666.09 for Landsat 7,
- K_2 = Band 10 thermal conversion constant from the metadata (Landsat 8) or 1282.71 for Landsat 7

Adding the absolute zero ~ -273.15 °C, is for converting from Kelvin degrees to Celsius degrees.

3. Land Surface Emissivity (LSE)

To better acquire LST estimates, it is important to know the ground emissivity or land surface emissivity (LSE (ελ)), which is the ability of a surface to transmit thermal energy to the atmosphere. It scales blackbody radiation according to Planck's law, to estimate the emitted radiation. It varies with vegetation conditions and surface roughness, which must also be known.

The Normalized Differential Vegetation Index (NDVI) is calculated following the formula:

$$NDVI = \frac{NIR - RED}{NIR + RED} \qquad (Eq.13)$$

where,

NIR and RED are the Near Infrared and Red bands respectively represented by NIR (Band 5) and RED (Band 4) in Landsat 8, and NIR (Band 4) and RED (Band 3) in Landsat 7.

Estimation of LSE requires knowledge of vegetation proportion *Pv* which is calculated from the following equation (Gemitzi A., and al., 2021):

$$Pv = \left(\frac{NDVI - NDVI_{min}}{NDVI_{max} - NDVI_{min}} \right)^2 \qquad (Eq.14)$$

where,

NDVImax corresponds to fully vegetated surfaces if is > 0.6 and *NDVImin* refers to bare soil if is < 0.18 (Gemitzi A., Delampakis P. and Falalakis G., 2021; Sobrino et al., 2004; Sobrino and Raissouni, 2000). From the *NDVI* result of study area, *NDVImin* value is -

0.00341793 and *NDVImax* value is 0.52948. Means that our study area is not totally covert by vegetation, it lies between a bare ground and a ground slightly covered with vegetation.

Next, LSE ($\varepsilon\lambda$) is the average emissivity of an element of the surface of the earth calculated from NDVI values using the equation:

$$\varepsilon\lambda = 0.004 * Pv + 0.986 \quad \textit{(Eq.15)}$$

where:

- $\varepsilon\lambda$ = Land Surface Emissivity (LSE)
- *Pv* = Proportion of Vegetation

4. Land Surface Temperature (LST)

The LST is the radiative temperature which calculated using Top of atmosphere brightness temperature, wavelength of emitted radiance, LSE using equation:

$$LST = \left(\frac{BT}{1}\right) + W * \left(\frac{BT}{14380}\right) * ln\,(\varepsilon_\lambda) \quad \textit{(Eq.16)}$$

where,

- BT = TOA brightness temperature (°C)
- W = Wavelength of emitted radiance (see table 3 above)
- $\varepsilon\lambda$ = Land Surface Emissivity (LSE)

The estimation of LST values with ASTER is done using the thermal band 14 according to the steps:

1. Radiometric calibration

The radiometric calibration is a module used to calibrate image data (Pixel value) to radiance, reflectance, or brightness temperatures. For this case, radiance has been chosen.

To calculate it, the ASTER thermal bands are selected, and the module takes gains and offsets for each band by reading their values from the sensor metadata using the following equation:

$$L\lambda = Gain * Pixel\ value + offsets \quad \textit{(Eq.17)}$$

where,

$L\lambda$ is Spectral radiance (W/(m2 * sr * μm))

2. Thermal Atmospheric Correction

After converting the thermal image data to radiance, atmospheric thermal correction is used to approximate and remove atmospheric contributions from the thermal infrared radiation data. It is done using the following equation (Harris A., 2013):

$$L(\lambda, T_s) = \frac{L(\lambda, T^*) - L_U(\lambda)}{\tau(\lambda)\,\varepsilon(\lambda)} \qquad \textit{(Eq.18)}$$

where,

- $L(\lambda, Ts)$: Radiance of a blackbody at the surface
- $L(\lambda, T^*)$: Radiance arriving to the sensor (corresponding to brightness temperature)
- $L_U(\lambda)$: Upwelling radiance from the atmosphere
- $\tau(\lambda)$: Transmissivity
- $\varepsilon(\lambda)$: Emissivity

ENVI uses an atmospheric correction algorithm that first determines the wavelength that most often has the maximum brightness temperature. This wavelength is then used as the reference wavelength. Only those spectra that have their brightest temperature at this wavelength are used to calculate the atmospheric compensation. At this stage, for each wavelength, the radiance values of the reference blackbody are plotted against the measured radiances. A line is fitted to the highest points in this plotted data and the fit is weighted to give more weight to regions with denser sampling. The compensation for this band is then applied as the slope and offset derived from the linear regression of these data with their calculated blackbody radiances at the reference wavelength. According to Harris Geospatial Solutions (2017), the atmospheric rise and transmission are the derivatives of the slope and offset of said line. This is first done when the surface temperature of each pixel is estimated from the data and used to estimate the brightness temperature using the Planck function and assuming an emissivity of 1. Then a line is fitted to a cloud of radiation points with respect to the brightness temperature. The atmospheric upwelling and transmission are then derived from the slope and offset of this line.

3. Emissivity normalization

After applying the atmospheric, thermal correction, emissivity normalization is used to calculate emissivity and temperature values from the thermal infrared radiation data. This technique calculates the temperature for every pixel and band in the data using a fixed emissivity value. With the Planck function, emissivity values are calculated using the highest temperature for each pixel.

For the thermal mapping in this study, we calculated the LST for thirteen satellite images. This LST corresponds to the temperature integrated over the pixel size of 30x30 m for Landsat (fig.24) and 90x90 m for ASTER.

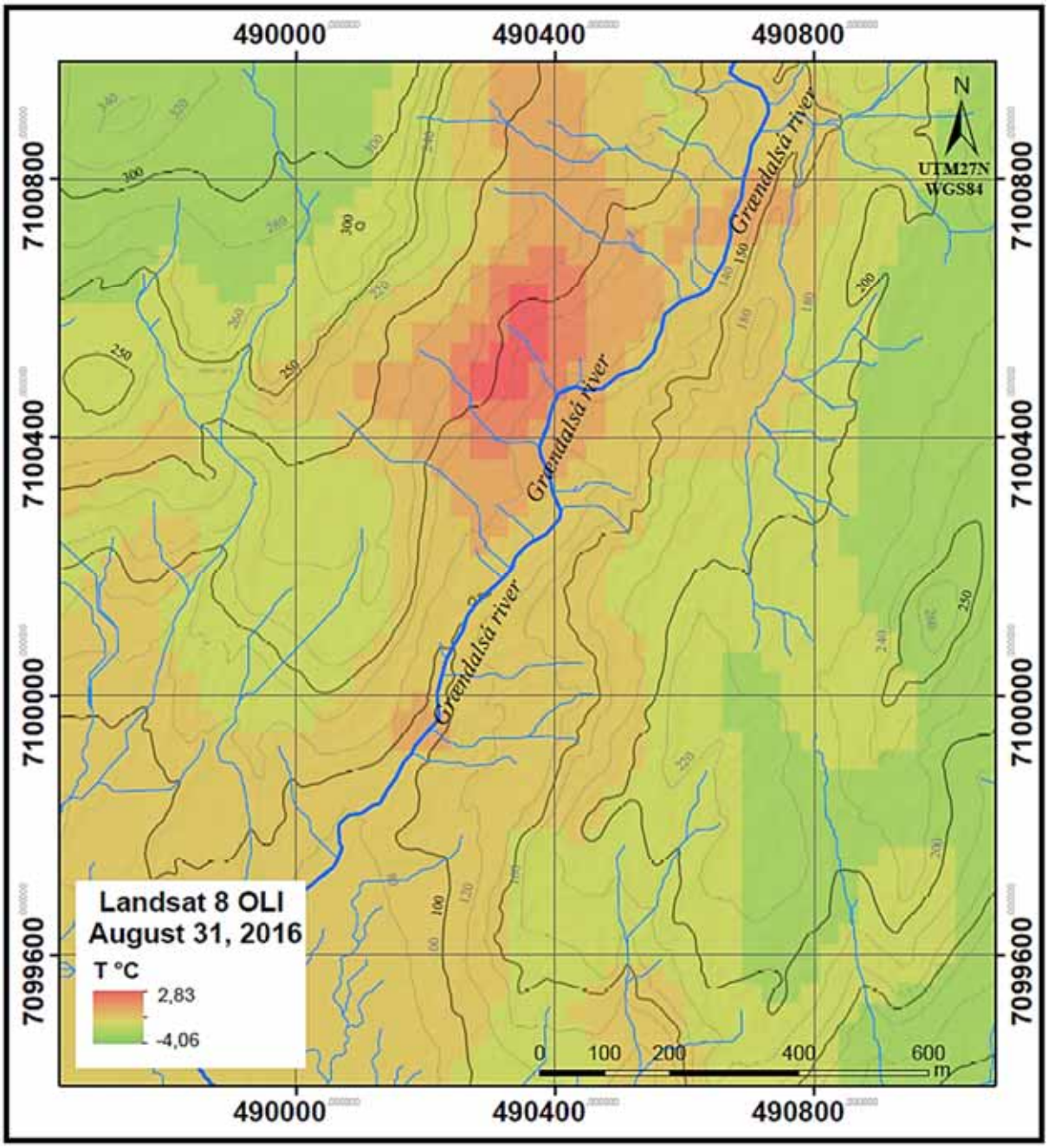

Figure 24: Kinetic LST of Grændalur valley derived from Landsat 8 OLI August 31, 2016, nighttime scene.

4.2.2 TIR camera carried by a drone

The use of drones has become one of the most important image acquisition tools in the world. In this study, we used the DJI Matrice 200 drone carrying the TIR camera Zenmuse XT by FLIR (fig.25).

Figure 25. The DJI Matrice 200 drone at Grændalur.

The TIR images acquired in GeoTIFF format by the drone were used for the identification of thermal anomalies over the Grændalur Valley. Several TIR images were taken on April 30, 2021 (afternoons when the sun was not present) over the selected area at 120 m altitude and at a 20 m flight line interval (fig. 26).

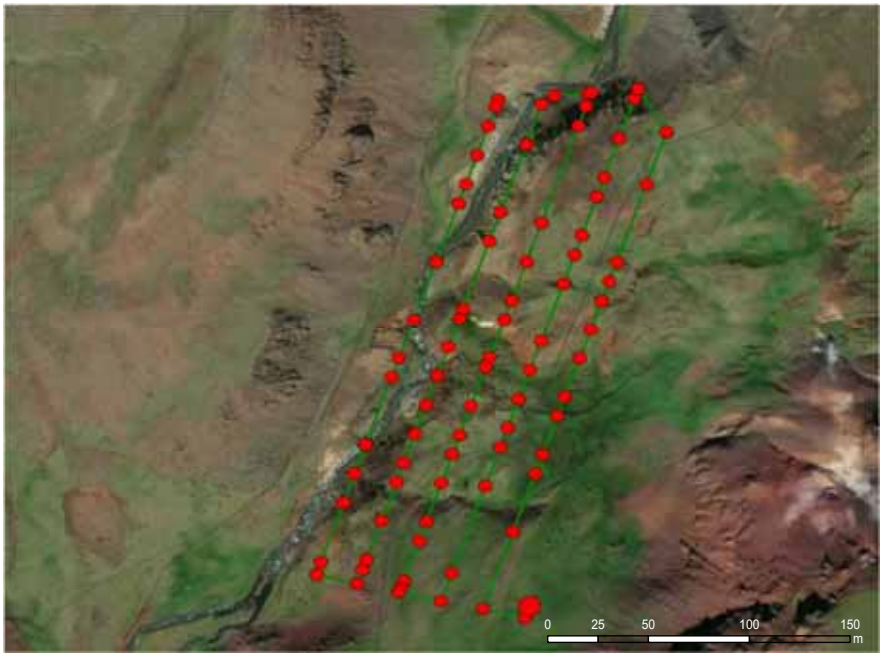

Figure 26. Flight line of the DJI Matrice 200 drone at Grændalur.

Some ground temperature measurements of the area covered by the TIR images were taken with a digital thermometer for the calibration of the TIR images. These measurements were taken directly after the flight, at around depth of 5 cm in the ground and in the water. GPS coordinates were taken at each measurement point.

The Universal Transverse Mercator (UTM) projection system precisely from zone 27 North and the World Geodetic System 1984 coordinate datum were used for the geographic positioning of these data. Data processing was done using ArcGIS 10.6 software.

Table 5 and 6 show the technical specifications of the TIR camera and the spatial resolution of the TIR images.

Table 5: Technical specifications of the TIR camera Zenmuse XT

Items	Specifications
Dimension	103 mm x 74 mm x 102 mm
Weight	270 g
Angular Vibration Range	±0.03
FPA/Digital Video Display Formats	640 x 512
Pixel Pitch	17 µm
Spectral Band	7.5 - 13.5 µm
Lens Model	13 mm
FOV	45° x 37°
IFOV	1.308 mr

Table 6: Spatial resolution of the TIR camera Zenmuse XT

Height of the camera	Image size (m)	Pixel size (cm)
120 m	94.248 x 77.496	14.754 x 15.122

The steps followed for thermal anomaly mapping using a TIR camera carried by a drone are shown in the figure 27.

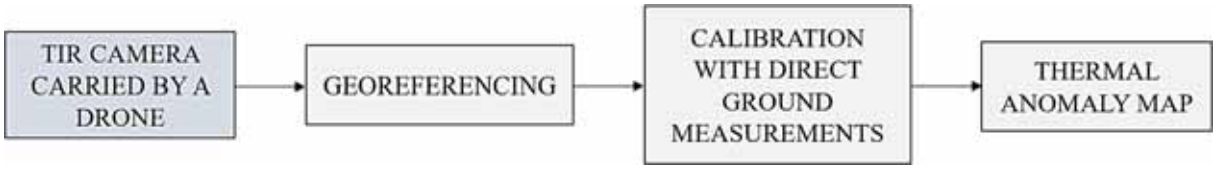

Figure 27: Steps followed for the thermal anomaly mapping using a TIR camera carried by a drone

5 Results and discussion

5.1 Geothermal mapping

In the Grændalur area, the geothermal manifestations listed are hot ground, warm ground, steam vents, mud pools, fumaroles, cold springs, warm springs, and hot springs. Among all these geothermal manifestations, the most abundant are the hot springs.

As shown by the topography in 2D and 3D view, the Grændalur region is at a relatively medium and low elevation (Figure 28).

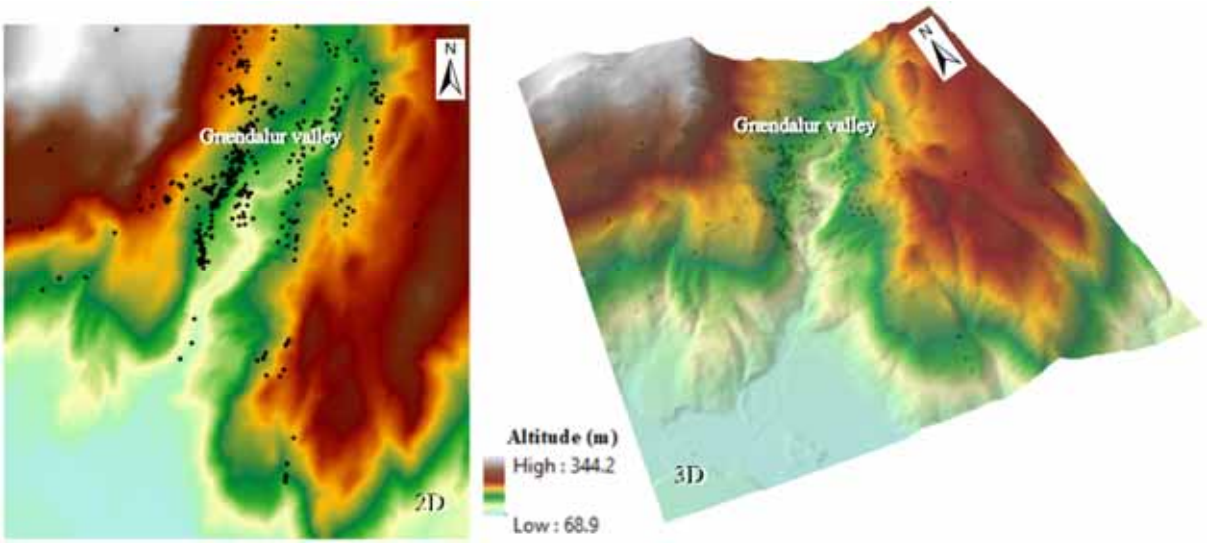

Figure 28: 2D and 3D view of the topography of Grændalur area. DEM from the www.lmi.is website. ArcMap (2D) and ArcScene (3D) of ArcGIS 10.6. The black and green dots are the geothermal manifestations described below.

5.1.1 Geothermal manifestations

a. Hot springs

In the Grændalur area, hot springs are the most abundant geothermal manifestations. These are sources that indicate a great geothermal activity in the region. They have a temperature above 50°C, some of which are boiling, and others are simply hot (fig.29). Some sources emit bubbles of CO_2 gas. The majority of these sources are colorless, others are whitish (coloring influenced by the presence of calcite) and others are brown (coloring influenced by the presence of clay particles). Around most of the hot springs, there are deposits of silica, calcite and copper (in some springs); however, other hot springs are new and there are no deposits around. These hot springs could be connected to or influenced by the level of groundwater in the area.

Figure 29: Hot spring in Grændalur.

b. Mud pools

Mud pools are geothermal manifestations that form in high temperature geothermal areas where water is scarce. In the Grændalur valley, the mud pools are near hot springs. They are characterized by greyish boiling mud in a small basin formed by the little water available in these areas.

c. Warm springs

In the study area, all springs with temperatures between 15 and 50°C have been classified as warm springs. They are located at slightly higher altitudes than the hot springs. Around these sources, there are deposits of calcite. These sources, could be meteoric waters which circulate in the fractures and, are then heated by the steam circulating in the fractures and the faults and cooled maybe by clay alterations or by a diminishing geothermal activity.

d. Cold springs

In the Grændalur valley, all sources with a temperature below 15°C are classified in the category of cold sources (fig.30). These sources can be groundwater that leans to the surface following fractures and faults. They are located at slightly higher altitudes than warm springs and hot springs.

Figure 30: Cold spring in Grændalur.

e. Fumaroles/steam vents

These different geothermal manifestations are often found together and are sometimes linked to each other in the same place. Fumaroles and steam vents are well known, often with a hissing sound. They occasionally occur along tiny cracks or long fissures in clusters or non-systematic fields. In active geothermal areas, there are fumarole / steam vents that emit steam and gases with different compositions, the most common contents are water vapor as dry steam (fig.31), H_2S and CO_2 and other gases. The fumaroles which emit sulphurous gas are called Solfatara (Italian term coming from solfo which means sulfur).

Figure 31: Dry steam in Grændalur.

f. Hydrothermal alteration, hot ground / steaming grounds and warm grounds

Generally, hydrothermal alteration is a process which occurs when there is interaction of a rock and a hydrothermal fluid, leading to the change of the physical and chemical components of the original rock by replacing its primary minerals with minerals secondary. Sampling the

temperature of the altered soil in the area allowed us to subdivide this altered soil into two groups.

- Hot grounds/steaming grounds are characteristic soils of a zone of high geothermal activity, the temperature of which is above 50°C. They are easily identified by their whitish-brown, brownish-red color with deposits of gypsum, calcite, aragonite, and silica. In the study area, the highest temperature in the area was 98.6°C (fig.32).

Figure 32: Steaming ground in Grændalur.

- Warm grounds occur in a geothermal area and their temperature is below 50°C. They are easy to identify especially from the color of the vegetation (the moss) which generally changes from green to yellowish when the temperature increases. And in areas that do not have vegetative cover, warm soils have moist surfaces of smooth clay and they are identified by a whitish coloration due to precipitation of calcite (Fig.33).

Figure 33: Yellowish green moss in warm ground in Grændalur.

5.1.2 Relationship between the surface manifestations and the geological structures

In a geothermal area, the characterization of geological structures is very important because these structures are often directly linked to geothermal manifestations. Generally, the information collected directly in the field and remote sensing allow us to observe and determine the direction of these structures. The analysis of the information collected in the Grændalur area from the remote sensing and the observation of the alignment of the geothermal manifestations (used as an indication for the presence of a geological structures), shows us that the faults and fractures found in this area have NE-SW, NS, EW, and NW-SE directions (fig.34).

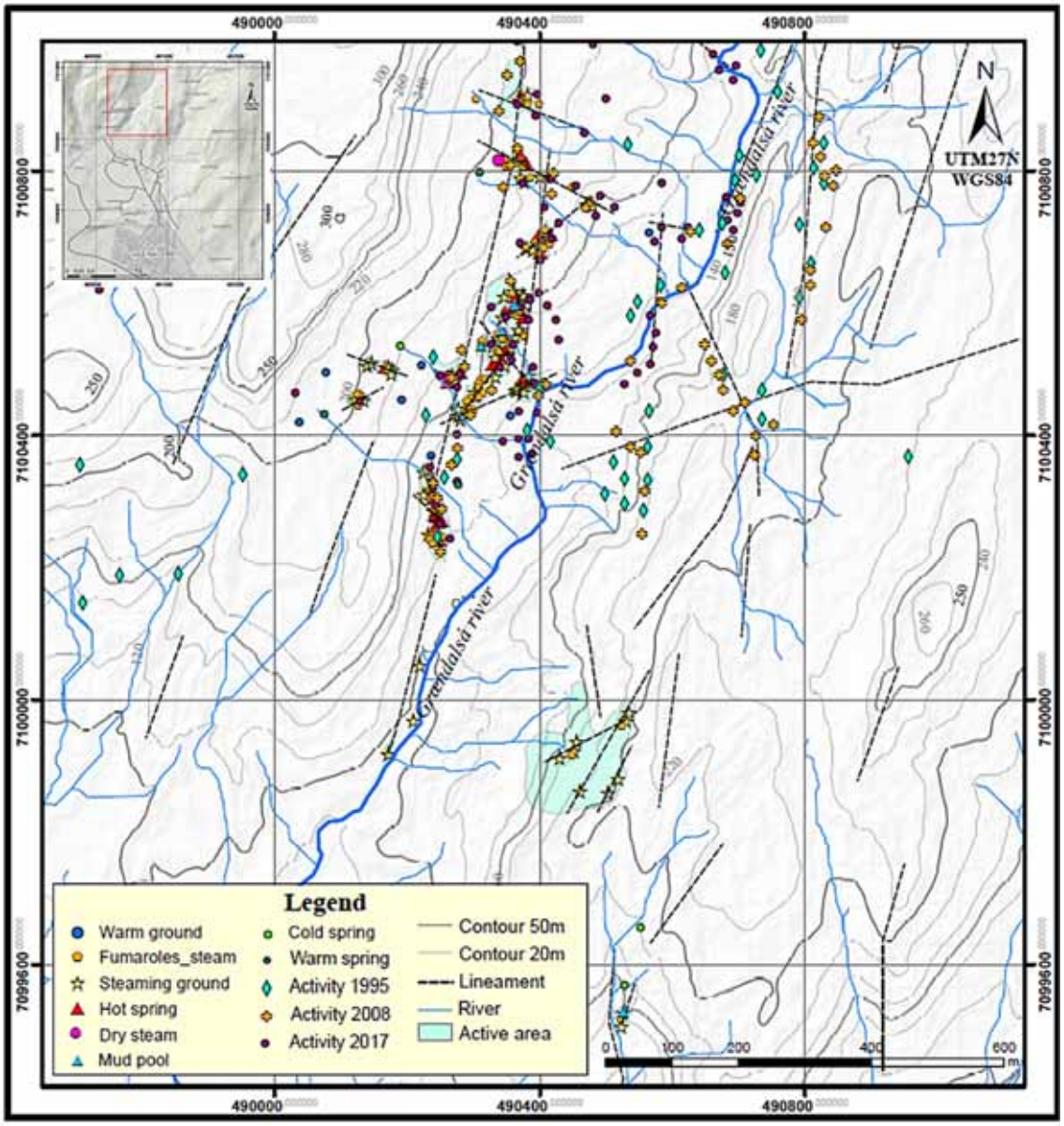

Figure 34: Geothermal mapping of Grændalur valley. Red rectangle showing the location of the area in the figure 1b.

As noted above, the geothermal manifestations found in the Grændalur are hot ground, warm ground, dry and steam vents, mud pools, cold springs, warm springs, and hot springs.

The figure 34 shows us the distribution of the different geothermal manifestations in the study area and we have subdivided them into 5 regions from de north to the south (B1, B2, B3, B4 and B5).

- ***Regions B1 and B2***

The distribution of geothermal manifestation in regions B1 and B2 is as follows (fig.35):

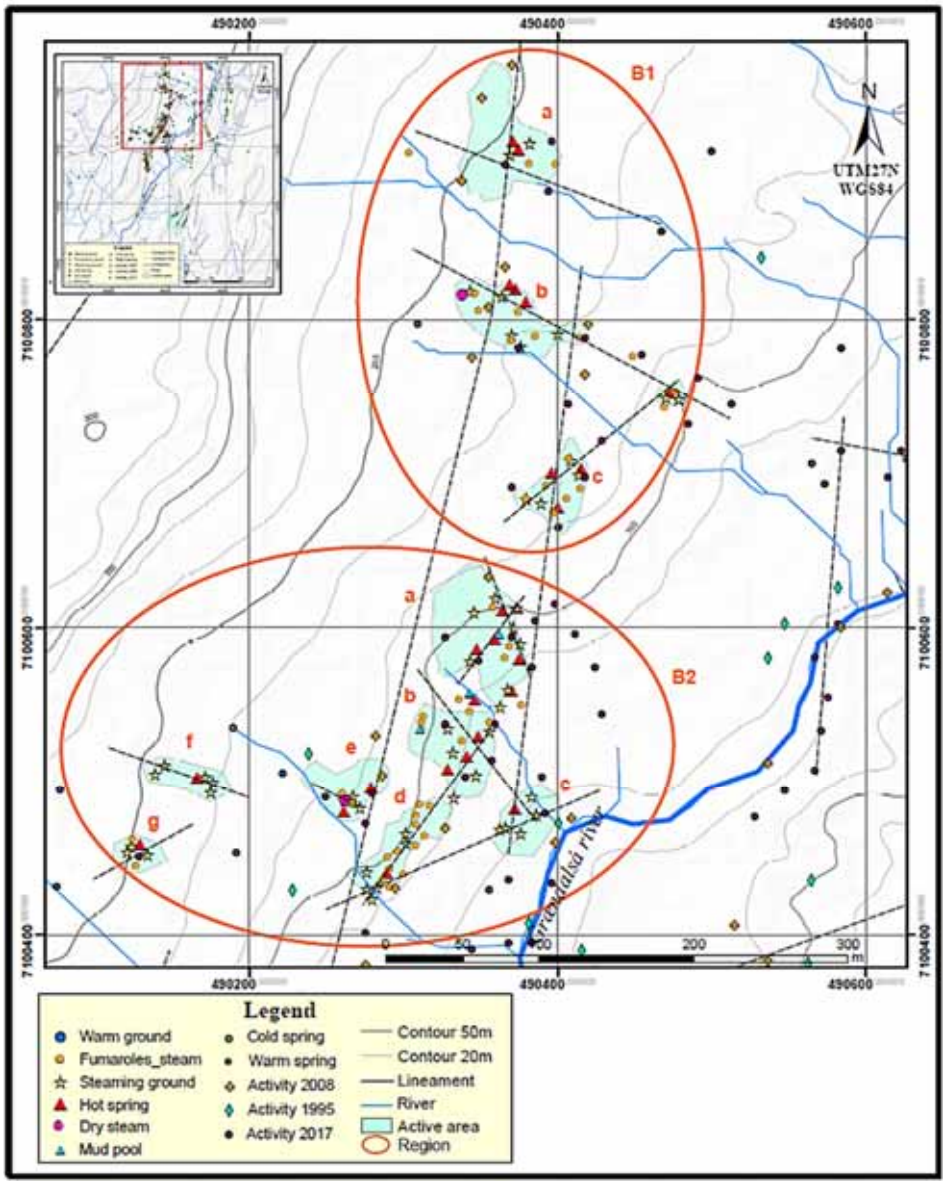

Figure 35: Geothermal manifestations and active geothermal areas in regions B1 and B2. Red rectangle showing the location of this area in the figure 34.

- In general, the geothermal manifestations are located on a slope in the region B1. In region B1a, on both sides we observe the boulder rock slides. The hot springs in this area have a temperature of around 78°C. There is also the fumaroles and the steaming ground which gives off an odor of sulfur (H_2S). The activity covers a

semi-circular area with a radius of about 35m. Green and yellowish green foam is found all around the steaming ground (fig.36). The geothermal manifestations follow a practically N-S direction in B1c and NW-SE direction in region B1b, there is a dry steam in this part which seems to be new.

Figure 36: Geothermal manifestations in region B1a.

- The region B2 is covered by an area of about 291x219m. Most geothermal manifestations in this region are grouped together in places, they are notably the steaming ground (surrounded by red-brownish, white and yellowish mineral precipitates) and the hot spring (with an average temperature of around 87°C) found in all the zones, there are fumaroles in zones B2a, B2b, B2d, B2e and B2g; the mud pools in regions B2a and B2b and the dry steam in the zone B2e. The geothermal manifestations follow a NW-SE and NE-SW direction. In zone B2a, yellowish green moss and dry grasses are easily observed, indicating new geothermal activity (fig.37). The area B2f, appears to be new.

Figure 37: Geothermal manifestations in region B2f.

- ***Regions B3, B4 and B5***

The distribution of geothermal manifestation in regions B3, B4 and B5 is as follows (fig.38):

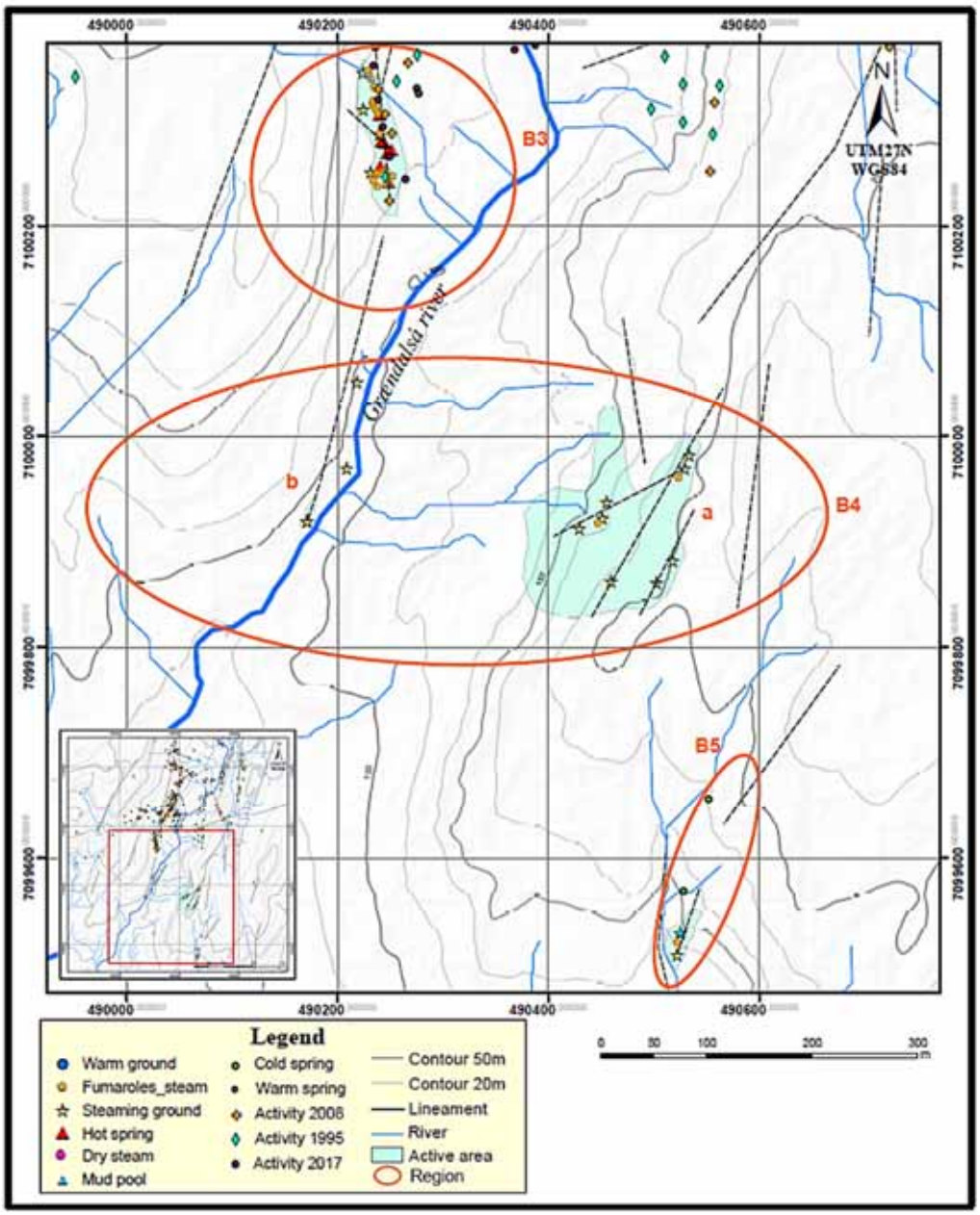

Figure 38: Geothermal manifestations, geological structures, and active geothermal areas in regions B3, B4 and B5. Red rectangle showing the location of this area in the figure 33.

- *Region B3*: it is an area of intense geothermal activity. These activities follow a practically NS direction and cover an area of about 150 x 25m. They are mainly composed of hot spring with a temperature around 98.2 °C, fumaroles, steaming grounds which are surrounded by deposits of white, yellowish and red-brownish minerals (fig.39).

Figure 39: Geothermal manifestations in region B3.

- *Region B4:* In this region, the geothermal events are the fumaroles and steaming grounds. In the B4a region, these manifestations are located on a steep slope and are cut off by a dike (fig.40). They are more remarkable for the color of the white mineral deposits that compose them. The B4b region is located on the small path which leads to the north of the site. The geothermal manifestations in this area are spaced along a N-S direction.

Figure 40: Geothermal manifestations in region B4.

- *Region B5:* In this region, geothermal manifestations are grouped together. The area covers an area of approximately 53 × 23 m. These geothermal manifestations follow a NE-SW direction. They are composed of steaming grounds with a temperature of 97.8°C and white, yellowish and red-brownish minerals, and fumaroles, one of which is directly connected to the mud basin above the slope. Next to the steaming grounds, there are green and yellowish-green moss (fig.41).

Figure 41: Geothermal manifestations in region B5.

Mapping of surface manifestations in the Grændalur valley, has revealed new manifestations that were created after major earthquakes of May 2008. Comparative analysis of the data presented in this thesis and previous work (before the earthquake described by Saemundsson, 1995 and after earthquake by Thorbjörnsson et al., 2009; and Gemechu E.A., 2017) showed that there was an increase in geothermal activity in the area in 2008 immediately after the earthquake. Geothermal manifestations such as hot springs, boiling springs, fumaroles/steam vents, warm grounds, hot grounds and steaming grounds were identified towards the slightly elevated areas. In some parts of the study area, the geological features are covered by surface deposits, but the geothermal activity has been powerful to manifest itself at the surface revealing subsurface geological information such as alignments NE-SW, NS, EW, and NW-SE directions.

5.2 Identification of thermal anomalies

5.2.1 Satellite based LST retrieval

The thermal mapping done in this study required the calculation of LST for eleven satellite images (Daytime and nighttime scenes).

The figure 42 shows the temperature values in degrees Celsius. In these different maps, the highest temperatures corresponding to the surface geothermal areas and are represented in red and orange values. They show us the time series of thermal anomalies in the Grændalur valley using Landsat and ASTER imagery.

These thermal maps cover the period from 2005 to 2020. The observation of these different maps shows us a certain evolution of the spatial distribution of the thermal anomalies with time. In the area, the evolution is remarkable by the decrease of high thermal anomalies with time.

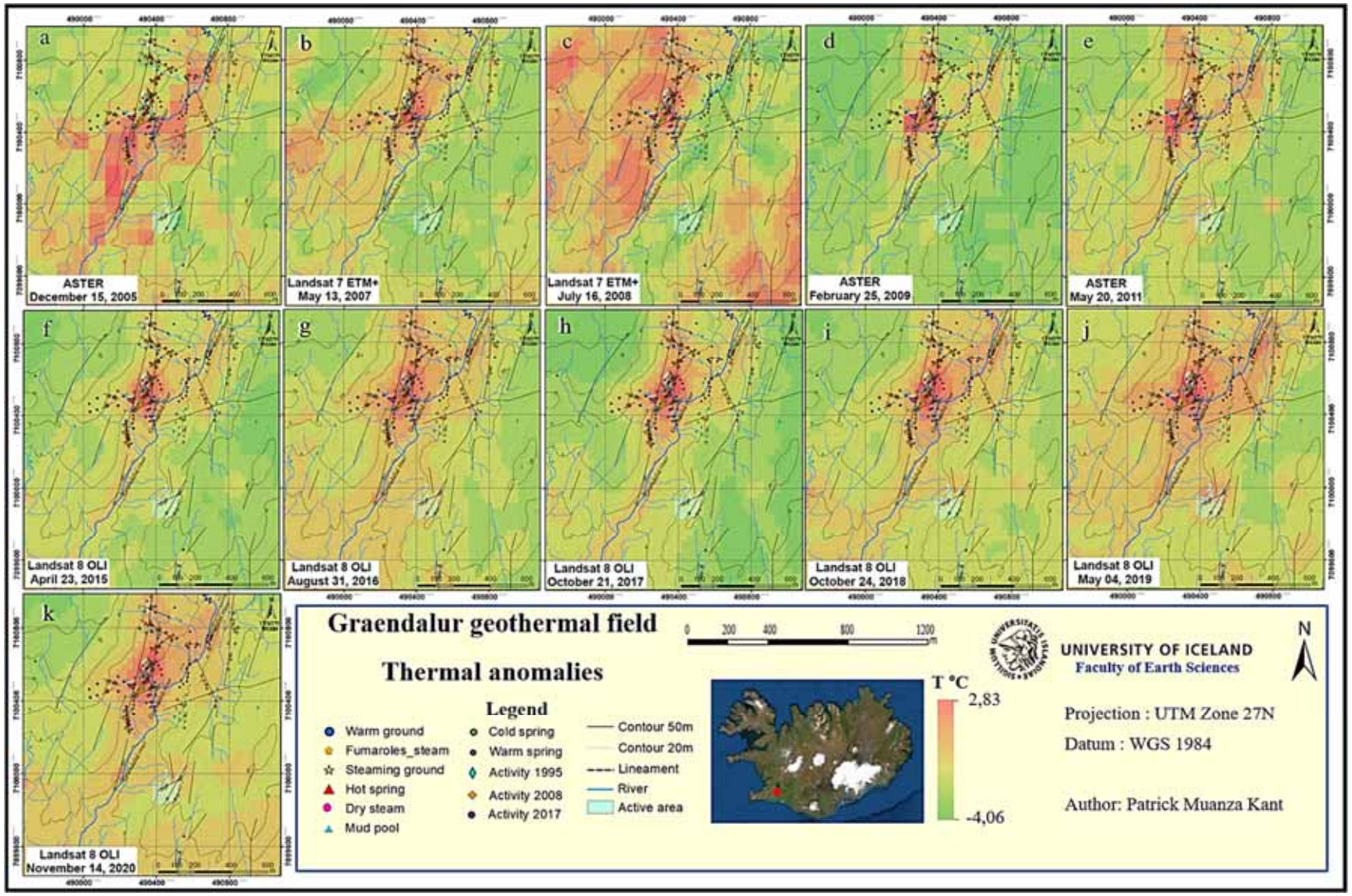

Figure 42: Evolution of thermal anomalies in the Grændalur geothermal field from 2005 to 2020. Thermal anomalies were categorized by standard deviations. The letters from a to k are related to the scenes (table 5 above).

Analysis of figure 43, which zooms in on the Grændalur region, shows us that a thermal anomaly in the north close to the center is not detected on December 15, 2005 during the nighttime and May 13, 2007 during the daytime, but it was detected on July 16, 2008 during the daytime and from February 25, 2009 to November 14, 2020 during the nighttime.

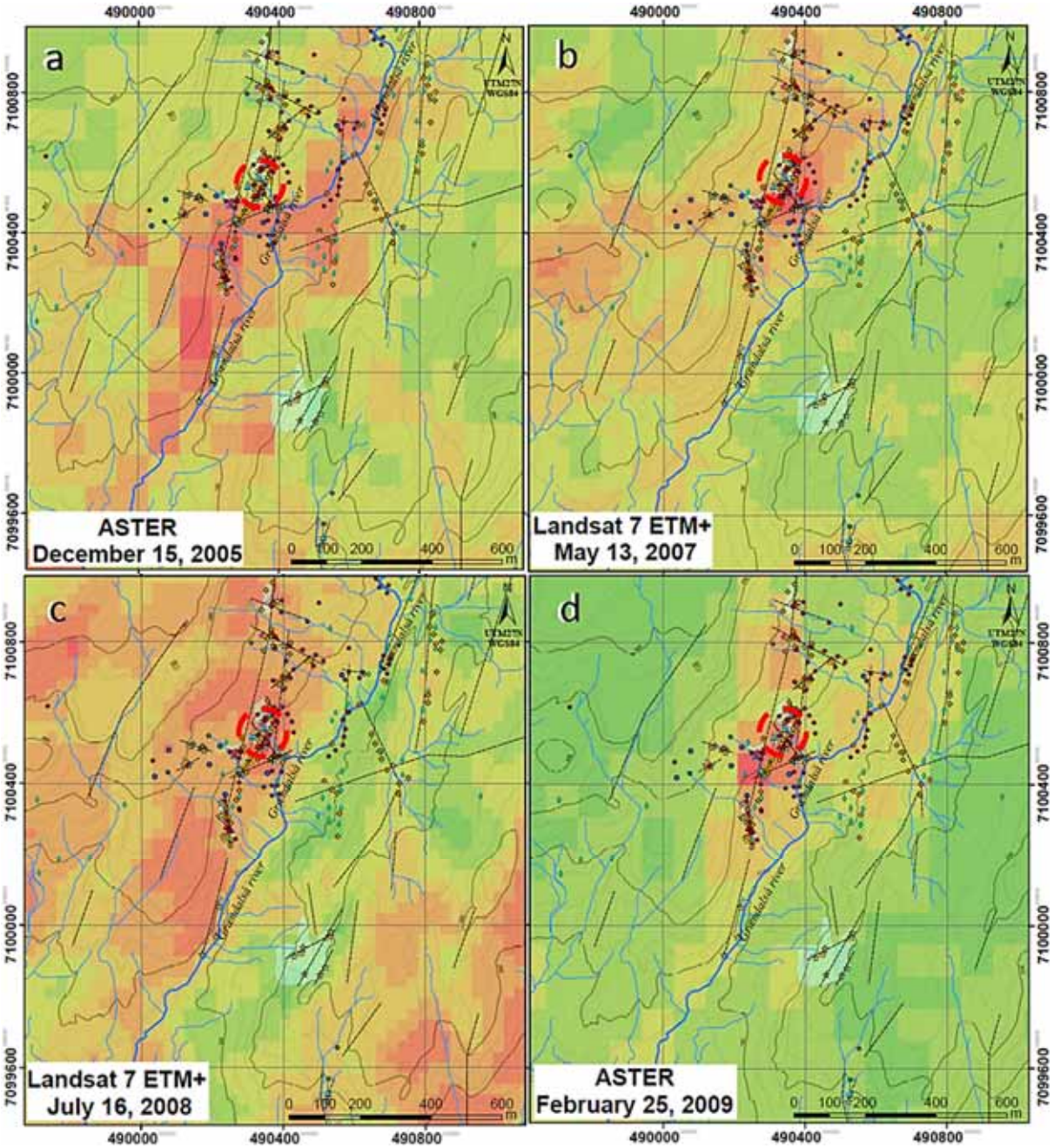

Figure 43: Thermal anomalies in the Grændalur geothermal field. The area where a thermal anomaly is not detected on December 15, 2005 and May 13, 2007 (within the red dotted line) (a and b) but detected from July 16, 2008 (c and d).

The thermal anomaly at Grændalur on December 15, 2005 and February 25, 2009 is not detected because the geothermal activity was not in that location at that time. This thermal anomaly seems to be a new geothermal activity that was created after the earthquake of May 29, 2008. As we said above, the date of May 29, 2008 was marked by an earthquake that had struck the region of Hveragerði (fig.6). And this earthquake had increased the geothermal

activity and revealed the presence of new geothermal manifestations in the area (Thorbjörnsson et al., 2009).

The estimation of the surface temperature made by the radiance analysis of the satellite images used in this study allowed us to identify the thermal anomalies on the valley of Grændalur. These different maps confirm the presence of geothermal manifestations and make the Grændalur valley one of the most active geothermal areas north of Hveragerði.

To better apply remote sensing to geothermal exploration, it is important to have an objective and specially to take into account the size of the target to be analyzed or sought.

Generally, from its spatial resolution, the satellite-based remote sensor detects, and records thermal anomalies produced in the Grændalur geothermal field. The analysis of the images taken at different times allows us to have a good understanding of the evolution of thermal anomalies over time in a region. But one of the difficulties during the research is that of finding good images without cloud during the day or the night. In this study, we had this problem. We did not find good images taken at night especially for the Landsat 7 ETM+, this led us to make a good selection of images taken during the day for the Landsat 7 ETM+ and during the night for the Landsat 8 OLI and ASTER.

5.2.2 TIR camera carried by a drone

Currently, the technology of image acquisition using cameras carried by drones has become essential. However, the good precision and reliability of the results require the control in situ. For this study, thermal images taken at 120 m height were acquired in TIFF format from the TIR camera Zenmuse XT carried on the DJI Matrice 200 drone. For a good accuracy, some ground temperature measurements with the digital thermometer and their GPS points were taken directly after the flight to calibrate the TIR images (table 7).

Before the TIR images were taken, the 120 m height RGB images were taken using the RGB camera Zenmuse X4S carried by the DJI Matrice 200 drone and the orthomosaic image was created using Pix4d Mapper. In total, 193 RGB images captured in 3 flights and 198 thermal images captured in two flights.

In the orthomosaic image, the steaming grounds in the southern part of the Grændalur valley are visible (Fig. 44).

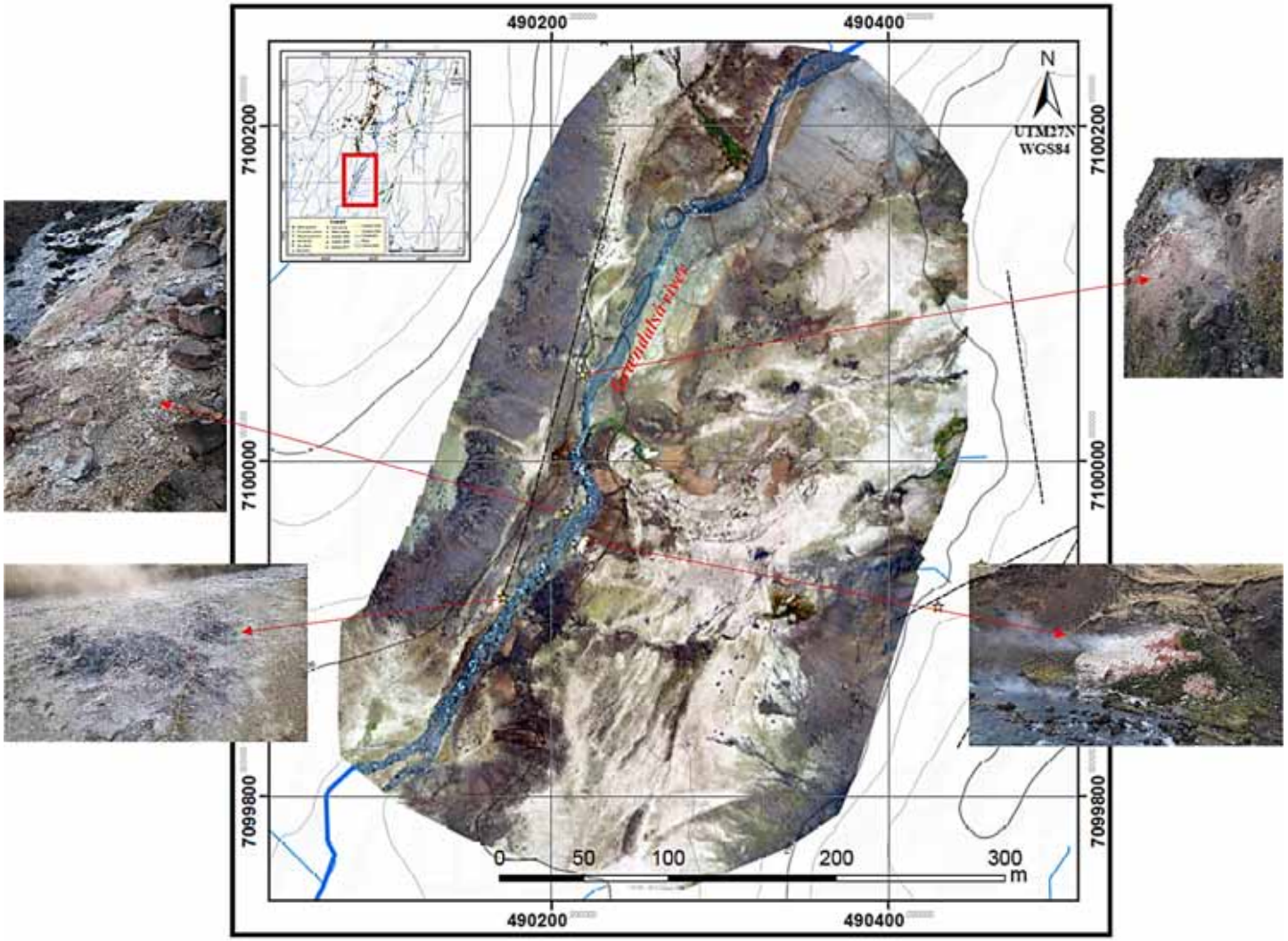

Figure 44: RGB mapping in the southern part of Grændalur valley showing the steaming grounds. Red rectangle showing the location of this RGB mapping in the figure 34.

Immediately after the RGB images were taken, the thermal images were taken with the TIR camera Zenmuse XT and then georeferenced using ArcGIS software. Figure 45 shows the thermal image, and the location of temperature measurement points (1-5) on the ground.

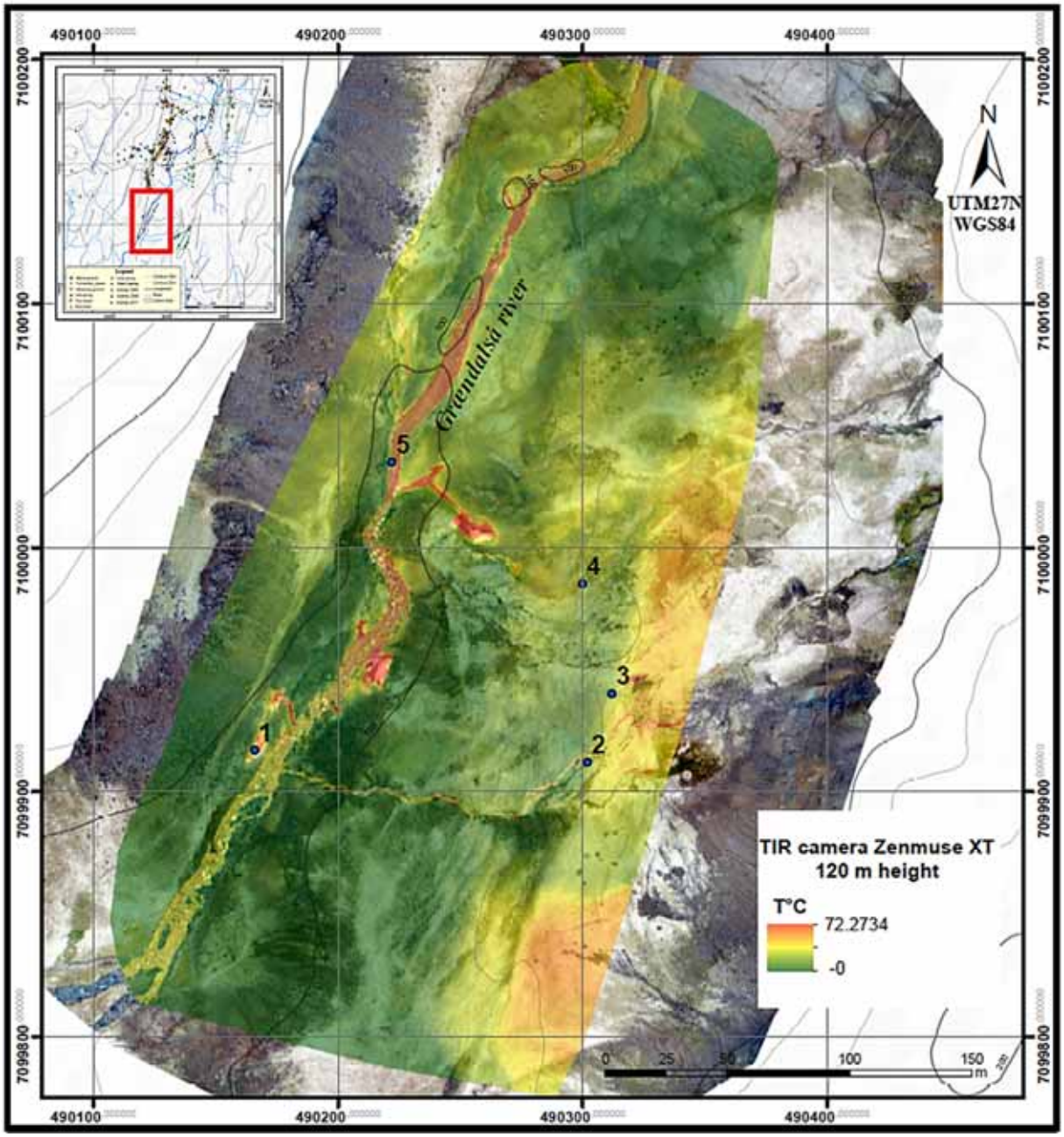

Figure 45: Thermal image taken with the TIR camera at 120 m. The blue labels are the locations where the direct temperature measurements were taken.

The temperature values of the thermal image pixels were then extracted using ENVI software at the same locations as the direct temperature measurements for the calibration (Table 5).

Table 7: Temperature measurements in the soil (water and steaming ground) and extracted from the TIR camera

Num.	Y_UTM/ 27N	X_UTM/ 27N	Direct temperature measurement (T°C)	Temperature from the TIR camera (T°C)	Station
1	7099917	490166	65	33.49	Steaming ground
2	7099912	490302	34.9	30.98	Warm spring
3	7099940	490312	6.7	9.53	Ground
4	7099985	490300	6	9.46	Ground
5	7100035	490222	17.3	19.06	River

The difference in temperature between the direct temperature measurement and that extracted from the thermal image can be explained by the pixel size which generally increases with height. Since geothermal manifestations generally cover small areas, a thermal image taken from at a high elevation will have a large pixel size, but the pixel temperature will be integrated.

The temperature values that were extracted from the thermal image were plotted against the measurements that were taken directly on the ground at 5 cm depth. The graph obtained from the plots shows the linear relationship between the temperature values extracted from the thermal image and the direct temperature measurements (Fig. 46). The highest temperatures in this graph correspond to warm water and steaming ground.

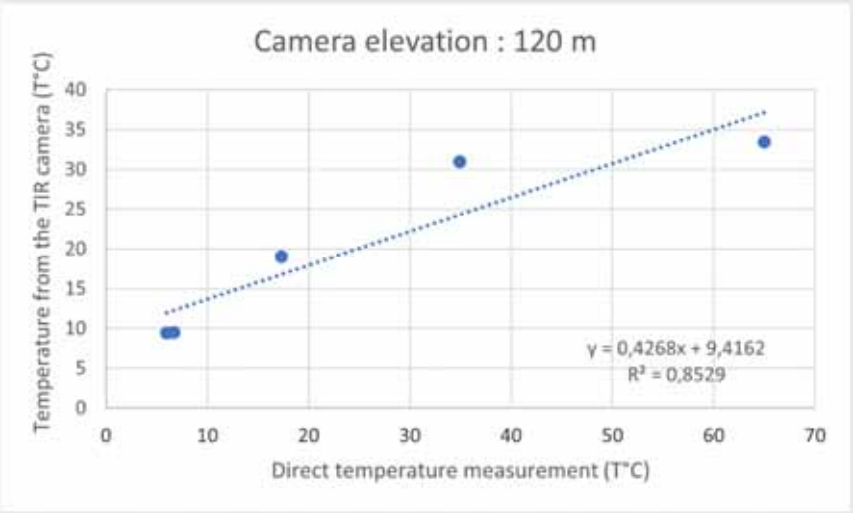

Figure 46: Plot of temperatures extracted from the thermal image at 120 m height and the direct temperature measurement at 5 cm.

The graph was made from Microsoft Excel and produced the linear regression equation with a coefficient of determination (R^2) of 0.85. This regression equation was used to calibrate the thermal image (Fig. 45).

Figure 47 shows the calibrated thermal image in degrees Celsius of the selected area with the highest temperature in degrees Celsius of about 43.6°C. These high temperature locations correspond exactly to steaming grounds that we observed in the field and visualized in the RGB image (fig.44). Also, to estimate the temperature of a geothermal manifestation located in a place where the accessibility is difficult because it is located on a steep slope.

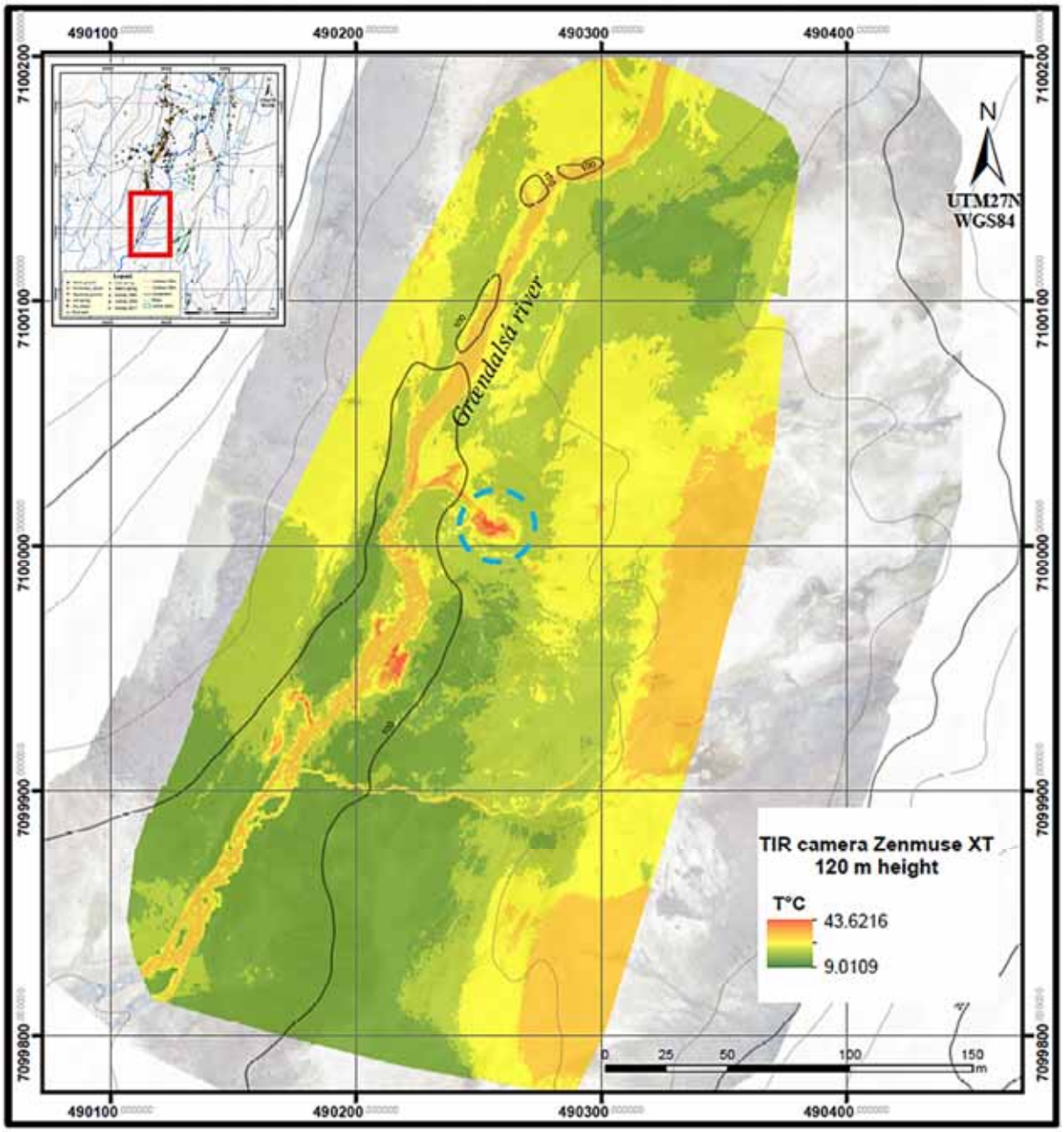

Figure 47: Thermal image calibrated taken with the TIR camera at 120 m. The blue dotted line is the geothermal manifestation located on a steep slope. Red rectangle showing the location of this thermal image in the figure 33.

In this thermal map, the highest temperature represented by the red value corresponds to the surface geothermal manifestations. The geothermal manifestation enclosed by blue dots shows the temperature pixel value of about 43°C at 120 m height.

The combined techniques of extracting land surface temperature from a satellite and a TIR camera carried by a drone produces effective results. It is used considering the size of the target to be detected. In the case of a geothermal area, geothermal manifestations such as steam vents, hot springs, mud pools, fumaroles, etc. that produce thermal anomalies are formed in small areas. In general, the size of these manifestations can vary from a few centimeters to a few

meters. These anomalies are easily detected at a distance by satellite from the spatial resolution of the sensor. For Landsat, the resolution of the thermal infrared (TIR) is 30 x 30m per pixel, for ASTER, it is 90 x 90m and for the TIR camera, it depends on the height at which the image is taken (at 120m height, the spatial resolution is 14.7 x 15.1 cm). It is difficult, if not impossible, for a geothermal manifestation to reach 30 or 90m in length to cover the pixel size of Landsat and ASTER as a whole. This means that the temperature value obtained from the Landsat and ASTER pixel is actually an integrated temperature. Compared to Landsat and ASTER, the TIR camera has much higher spatial resolution and the size of the geothermal manifestation can cover its pixel size if the image is taken at a good height.

These techniques cannot determine the type of geothermal manifestations found in the study area. Generally, the satellite produces images on a regular basis. These images contain information about the time they were taken. The careful analysis of the images taken at different times allows to understand the evolution of the geothermal activity of the studied region. The analysis of satellite images from 2005 to 2020 of the Grændalur valley, shows us a certain the decrease of high thermal anomalies with time (Fig. 41). This decrease of the observed surface high thermal anomalies would be due to the decrease of the geothermal energy transfer to the surface. A thermal anomaly in the center near the north was not detected until 2008 on the ASTER image nor on Landsat 7 ETM+. This anomaly has been detected since 2008 until 2020 on ASTER, Landsat 7 ETM+ and Landsat 8 OLI. It would have appeared after the earthquake of May 29, 2008.

To better monitor the possible change of geothermal activity (appearance or extinction of a geothermal manifestation) of an area, it is better to use remote sensors with a higher spatial resolution such as a thermal camera carried on a drone. The images produced by a thermal camera carried on the drone provide more detailed information because they can be taken at different altitudes. Regularly taking images from the thermal camera allows for careful monitoring of changes in geothermal activity and estimation of surface temperature after calibration with data taken in the field. In the Grændalur valley, the TIR image taken by a camera carried on the drone at 120m was calibrated with temperature measurements taken directly on the ground at 5cm depth. This calibrated TIR image was used to estimate the surface temperature (43°C) of a geothermal manifestation located in a difficult to access area (fig.46).

This combined technique was used in the Sveifluháls-Krýsuvík high temperature Geothermal field to analyze time series of thermal anomalies from 2002 to 2017 and calculate the radiative heat flux (Ramírez-González L.M. et al., 2019).

6 Conclusions

Geothermal exploration is one of the important phases in the development of a geothermal project. One of the most important methods of geothermal exploration is the geological investigation method. This method is done by two direct and indirect approaches. The direct approach requires a field trip to make detailed maps, among which is the geothermal mapping. The indirect approach is the spatial analysis using remote sensing.

The geothermal mapping of the Grændalur valley reveals that:

- the geothermal manifestations found in the area are hot springs, warm springs, fumaroles/steam vents, mud pools, hydrothermal alteration, hot ground, steaming ground and warm grounds.

- The geothermal manifestations in the area follow NE-SW, N-S, E-W, and NW-SE oriented alignments that inform us about the direction of faults and fractures covered by the surface deposits.

The processing of TIR bands of Landsat and ASTER satellite images covering the period from 2005 to 2020 and the thermal image taken by a camera carried on the drone, allowed to analyze the spatial and temporal distribution of surface thermal anomalies in the Grændalur valley. The results obtained allowed us to:

- identify the presence of a thermal anomaly that did not exist before the year 2008. This anomaly certainly appeared after the earthquakes of May 29, 2008 which had opened the door to a new geothermal manifestation and closed the door to others that existed in the area.

- identified and estimated at about 43°C the temperature of a thermal anomaly existing in an area located on a steep slope in the southern part of the Grændalur valley from TIR images with high spatial resolution taken by a TIR camera carried on the drone at 120m high.

This study attests to the importance of geothermal mapping, which is one of the most important early phases in geothermal exploration, which allows the study and mapping of geothermal manifestations and their correlation with geological structures for better understanding of the geothermal activity of a region. Also, it demonstrates the effectiveness of the analysis, processing and use of combined techniques of extraction of TIR images from satellite space sensors at different resolutions, taken at different times and that of the TIR image taken from the TIR camera carried on the drone in a geothermal area. This combination allows to cover large areas and detect thermal anomalies provided by geothermal manifestations.

The acquisition and regular analysis of these TIR images allow to monitor with great attention the possible changes of the surface geothermal activity in a geothermal area, especially for those located in a seismic area.

This combined technique can also be applied to the monitoring of an active volcano, by regularly analyzing TIR images of the volcanic area to detect possible changes in thermal anomalies provided by geothermal manifestations located in the area. These can provide information about a possible magma upwelling.

References

Allis R. G., Nash G.D. and Johnson S.D., 1999: Conversion of thermal infrared surveys to heat flow: Comparisons from Dixie Valley, Nevada, and Wairakei, New Zealand. *GRC Transactions* 23.

Ármannsson H., Kristmannsdóttir H., Torfason H., Ólafsson M., 2000: Natural Changes in Unexploited High-Temperature Geothermal Areas in Iceland. National Energy Authority, Orkustofnun, Reykjavik. *Proceedings World Geothermal Congress* 2000, Kyushu-Tohoku, Japan, May 28-June 10, 2000, 521–526.

Árnadóttir T., Geirsson H. and Einarsson P., 2004: Co-seismic stress changes and crustal deformation on Reykjanes peninsula due to triggered earthquakes in June 2000. *J. Geophys. Res. 109-B09307*, 12 pp.

Árnadóttir T., Geirsson H., and Jiang W., 2008: Crustal deformation in Iceland: Plate spreading and earthquake deformation. *Jökull, 58*, 67 pp.

Árnason and Gíslason, 2009: Geothermal surface exploration. Presented at "Short Course on Surface Exploration for Geothermal Resources", organized by *UNU-GTP and LaGeo*, in Ahuachapan and Santa Tecla, El Salvador.

Arnórsson S., 1995a: Geothermal systems in Iceland; structures and conceptual models I, high temperature areas. *Geothermics, 24,* 561-602.

Arnórsson S., 1995b: Geothermal systems in Iceland: Structure and conceptual models II. Low temperature areas. *Geothermics, 24*, 603-629.

Axelsson G., Björnsson G., Egilson T., Flóvenz O. G., Gautason B., Hauksdóttir S., Ólafsson M., Smárason O. B. and Sæmundsson K., 2005: Nature and properties of recently discovered hidden low-temperature geothermal reservoirs in Iceland. *Proceedings World Geothermal Congress* 2005, Antalya, Turkey, 24-29 April 2005, 10 p.

Bakker H.W., Gieske M.S. and Gorte B.G.H., 2004: Principles of Remote Sensing. *International Institute for Geo-Information Science and Earth Observation*, 2004.

Bakx W., Tempfli K., Tolpekin V., Woldai T., 2012: The Core of GIScience: a systemsbased approach. Chapter 2-Physics, 71-84. University of Twente, *International Institute for Geo-Information Science and Earth Observation (ITC)*, Enschede, The Netherlands.

Björnsson G., Flovenz Ó.G., Saemundsson K. and Einarsson E.H., 2001: Pressure changes in Icelandic geothermal reservoirs associated with two large earthquakes in June 2000. *Proceedings, Twenty-Sixth Workshop on Geothermal Reservoir Engineering, Stanford University, Stanford, California*, 29-31 January 2001.

Bodvarsson G., 1961: Physical characteristics of natural heat resources in Iceland. *State Electricity Authority*, Reykjavik, Iceland, G/6, 82-89.

Brandsdóttir B., Parsons M., White R.S., Gudmundsson O., Drew J. and Thorbjarnardóttir B.S., 2010: The May 29th, 2008 earthquake aftershock sequence within the South Iceland Seismic Zone: Fault locations and source parameters of aftershocks, 2008, *Jökull, 60,* 23-46.

Clifton A.E., and Einarsson P., 2005: Styles of surface rupture accompanying the June 17 and 21, 2000 earthquakes in the South Iceland seismic zone. *Tectonophysics*, 396, 159 pp.

Dech SW, Tungalagsaikhan P, Preusser C, and Meisner RE., 1998: Operational value-adding to AVHRR data over Europe: methods, results, and prospects. *Aerosp Sci Technol* 2:335–346

Einarsson P., 1991: Earthquakes and present-day tectonism in Iceland. *Tectonophysics, 189,* 261-279.

Einarsson P. 2008: Plate boundaries, rifts and transforms in Iceland. *Jökull, 58*, 35-58.

Einarsson P., Björnsson S., Foulger G., Stefánsson R., and Skaftadóttir T., 1981: Seismic pattern in south Iceland seismic zone. In; Simpson, D. and Richards. P. (eds.), *Earthquakes prediction – An international review, Am. Geophys. Union, Maurice Ewing Series 4,*151 pp.

Einarsson P., and Eiríksson J., 1982: Earthquake fractures in district and Rangárvellir in south Iceland seismic zone. *Jökull, 32*, 113-119.

Einarsson P., Böttger M., and Thorbjörnsson P., 2002: *Faults and fractures of south Iceland Seismic zone near Thjórsá*. Landdsvirkjun, Reykjavík, report LV-2002/090, 8pp.

Eneva M., Coolbaugh M. and Combs J., 2006: Application of Satellite Thermal Infrared Imagery to Geothermal Exploration in East Central California. *GRC Transactions* 30.

Eneva M., Coolbaugh M. F. and Bjornstad S. J., 2007: In search for thermal anomalies in the coso geothermal field (California) using remote sensing and field data. *Thirty-Second Workshop on Geothermal Reservoir Engineering, Stanford University*, Stanford, California.

Fridleifsson B. I., 1979: Geothermal Activity of Iceland. National Energy Authority, Reykjavik. *Jökull* 29. ÁR 47.

Fridriksson T., 2009: Diffuse CO_2 degassing through soil and geothermal exploration. Presented at "Short Course on Surface Exploration for Geothermal Resources", organized by *UNU-GTP and LaGeo*, in Ahuachapan and Santa Tecla, El Salvador, 17-30 October, 2009.

Gemechu E.A., 2017: Geothermal exploration in Grændalur valley, Hveragerði, S-Iceland. Report 11 in: *Geothermal training in Iceland 2017.* UNU-GTP, Iceland.

Gemitzi A., Delampakis P. and Falalakis G., 2021: Detecting geothermal anomalies using Landsat 8 thermal infrared remotely sensed data. International Journal of Applied Earth Observation and Geoinformation, Volume 96, April 2021, 102283.

Gudmundsson M.T., and Jacoby, W., 2007: Hotspot Iceland: An introduction. *J. Geodynamics, 43-1*, 1-5.

Hardarson, B.S., Fitton, J.G., and Hjartarson, A., 2008: Tertiary volcanism in Iceland. *Jökull, 58,*161-178.

Hardarson B.S., Fitton J.G., Ellam R.M., and Pringle M.S., 1997: Rift relocation-a geochemical and geochronological investigation of a paleo-rift in northwest Iceland. *Earth Planet. Sci. Lett., 153,* 181-196.

Harvey C. and al., 2013: Geothermal exploration best practices: a guide to resource data collection, analysis, and presentation for geothermal projects. *c/o Bochum University of Applied Sciences (Hochschule Bochum) Lennershofstr*. 140, D-44801 Bochum, Germany.

Haselwimmer C. E. and Prakash A., 2011: Use of airborne thermal imaging to quantify heat flux and flow rate of surface geothermal fluids at Pilgrim Hot Springs, Alaska. *AGU Fall Meeting* 2011, San Francisco.

Heasler H. P., Jaworowski C. and Foley D., 2009: Geothermal systems and monitoring hydrothermal features. *Geological Monitoring*. 105-140.

Ingólfsson Ó., Sigmarsson O., Sigmundsson F., and Símonarson L., 2008: The dynamic geology of Iceland. *Jökull, 58*, 1–2.

Jiang C.Y.H., 2013: Digital Elevation Model and Satellite Imagery Based Bushfire Simulation, *American Journal of Geographic Information System*, Vol. 2 No. 3, 2013, pp. 47-65. doi: 10.5923/j.ajgis.20130203.03

Kyagulanyi D., 1996: Geothermal exploration in the Hveragerði - Graendalur area, SW-Iceland. Report 8 in: *Geothermal training in Iceland 1996*. UNU-GTP, Iceland, pp. 161-176.

Kienholz C., Prakash A. and Kolker A., 2009: Geothermal Exploration in Akutan, Alaska, Using Multitemporal Thermal Infrared Images. American Geophysical Union, *Fall Meeting* 2009, abstract #H53F-1009.

Kratt C., Calvin W. and Coolbaugh M., 2006: Geothermal exploration with Hymap hyperspectral data at Brady–Desert Peak, Nevada. *Remote Sensing of Environment* **104**(3): 313-324.

Kratt C., Coolbaugh M. F. and Calvin W. M., 2006: Remote Detection of Quaternary Borate Deposits with ASTER Satellite Imagery as a Geothermal Exploration Tool." *GRC Transactions* **30**.

Kuenzer C., and Dech S., 2013: Remote Sensing and Digital Image Processing. *Chapter 1-Theoretical Background of Thermal infrared Remote Sensing*, 1-28. doi:10.1007/978-94-007-6639-6_1.

Leakey O., 2013: Overview of geothermal surface exploration methods. Organized by *UNU-GTP, GDC and KenGen*, at Lake Bogoria and Lake Naivasha, Kenya, Oct. 31 – Nov. 22, 2013.

Littlefield E. and Calvin W., 2009: Remote Sensing for Geothermal Exploration Over Buffalo Valley, NV." GRC Transactions **33**: 495-499.

Littlefield E. and Calvin W., 2010: Geothermal Exploration using AVIRIS Remote Sensing Data over Fish Lake Valley. *GRC Transactions* **34**: 599-603.

Magali Ramírez-González L.M., Aufaristama M., Jónsdóttir I., Höskuldsson Á., Þórðarson Þ., Proietti N.M., Kraft G. and McQuilkin J., 2019: Remote sensing of surface Hydrothermal Alteration, identification of Minerals and Thermal anomalies at Sveifluháls-Krýsuvík high-temperature Geothermal field, SW Iceland. *IOP Conf. Series: Earth and Environmental Science 254 (2019) 012005.* doi:10.1088/1755-1315/254/1/012005

Manzella A., 2017: Geothermal energy. *EPJ Web of Conferences* 148, 00012 (2017). DOI: 10.1051/epjconf/20171480.

Mburu M., 2014: Geothermal energy utilisation. Presented at Short Course IX on Exploration for Geothermal Resources, *organized by UNU-GTP, GDC and KenGen*, at Lake Bogoria and Lake Naivasha, Kenya, Nov. 2-23, 2014.

McDougall I., Kristjánsson L., and Saemundsson K., 1984: Magnetostratigraphy and geochronology of northwest Iceland. *J. Geophys. Res., 89(B8),* 7029-7060.

Mongillo M., 1994: Aerial Thermal Infrared Mapping of the Waimangu-Waiotapu Geothermal Region, New Zealand." *Geothermics* **23**(5/6): 511- 526.

Moorbath S., Sigurdsson H., and Goodwin R., 1968: K-Ar ages of oldest exposed rocks in Iceland: *Earth and Planetary. Science Letters, 4*, 197-205.

Munasinghe M.M.T.N.B., 2013: Geothermal exploration in Gufudalur, Hveragerði, SW-Iceland. Report 21 in: *Geothermal training in Iceland 2013*. UNU-GTP, Iceland, 477-500.

Özkaya U., Seyfi L., and Yaldız E., 2018: Analysis of Electromagnetic Radiation in Daily Life. SETSCI *Conference Indexing System*, Volume 3 (2018), 505-509.

Pagli C., Pedersen, R., Sigmundsson F., and Feigl K.L., 2003: Triggered fault slip on June 17, 2000 on the Reykjanes Peninsula, SW Iceland captured by radar interferometry. *Geophys. Res. Lett., 30-6,* 1273.

Pipan, 2009: Remote sensing and geophysical methods for geothermal exploration*.* Presented at the School on Geothermics, organised by *ICTP, ICS-UNIDO and IAEA*, Trieste, Italy.

Ragnarsson Á., 2015: Geothermal development in Iceland 2010-2014. *Proceedings of the World Geothermal Congress 2015, Melbourne, Australia*, 15 pp.

Rockwell B. W. and Hofstra A. H., 2008: Identification of quartz and carbonate minerals across northern Nevada using ASTER thermal infrared emissivity data—Implications for geologic mapping and mineral resource investigations in well-studied and frontier areas." *Geosphere* **4**(1): 218-246.

Sabins F. F., 1999: Remote sensing for mineral exploration. Ore Geology Reviews 14, 157–183.

Saemundsson K., 1967: Vulkanismus und Tektonik des Hengill-Gebietes in Sudwest-Island. *Acta Nat. Isl., II-7, (in German)*, 195 pp.

Saemundsson K., 1978: Fissure swarms and central volcanes of the neovolcanic zones of Iceland. *Geol. J., Sp. Issue, 10*, 415-432.

Saemundsson K., Axelsson G., and Steingrímsson B., 2009: Geothermal systems in global perspective. *Proceedings of a "Short Course on Surface Exploration for Geothermal Resources", organized by UNU-GTP and LaGeo, Santa Tecla, El Salvado*r, UNU-GTP, SC-09, 16 pp.

Saemundsson K., and Fridleifsson G.Ó., 1992: *The Hveragerði central volcano, geological description.* Orkustofnun, Reykjavík, report OS-92063/JHD-35 B (in Icelandic), 25 pp.

Saemundsson K., Þórólfur H. Hafstað og Freystein Sigurðsson 1994: Hveragerði og nágrenni. Jarðfræði-, jarðhita- og grunnvatnskort 1:5.000. Orkustofnun. Unnið fyrir Hveragerðisbæ.

Saemundsson K., 2009: Geothermal systems in global perspective. Iceland GeoSurvey (ÍSOR). *Presented at Short Course IV on Exploration for Geothermal Resources*, UNU-GTP, KenGen and GDC, Lake Naivasha, Kenya, November 1-22, 2009, 11p.

Sanderson R, 2014: Introduction to remote sensing. *GeoJournal, May 1982* DOI: 10.1007/BF00210657.

Scherer G. J., Riley D. N., Peppin W. A., Tratt D. M., Wright C. and Jones K. L., 2009: Geothermal Exploration with Visible through Long Wave Infrared Imaging Spectrometers. *Clean Technology* 2009. Houston, Texas.

Stefánsson R., Gudmundsson G. and Halldórsson P., 2003: *South Iceland earthquakes 2000- a change for earthquakes prediction.* Meteorological Office, Reykjavík, report VI-R03017, 21pp.

Stefánsson V. and Steingrímsson B., 1980: Geothermal logging: An introduction to techniques and interpretation. *Orkustofnun, National Energy Authority,* Rapport OS80017/JHD09, Reykjavik, May 1980.

Taranik, J. V., Coolbaugh M. F. and Vaughan R. G., 2009: An Overview of Thermal Infrared Remote Sensing with Applications to Geothermal and Mineral Exploration in the Great Basin, Western United States. *In Reviews in Economic Geology*, v.16, : Remote Sensing and Spectral Geology. R. Bedell, A. Crosta and E. Grunsky. Littleton, CO, Society of Economic Geologists Inc.

Thorbjörnsson D., Saemundsson K., Kristinsson S.G., Kristjánsson B.R, and Ágústsson K, 2009: *Southern lowland earthquakes May 29th, 2008, effect of groundwater level, geothermal activity and fractures*. ÍSOR – Iceland GeoSurvey, Reykjavík, report ÍSOR-2009/028 (in Icelandic), 42 pp.

Thórdarson T. and Larsen G., 2007: Volcanism in Iceland in historical time: Volcano types, eruption styles and eruptive history. Journal of Geodynamics 43, 118-152.

Thórdarson T., and Höskuldsson A., 2002: Classic Geology in Europe 3: Iceland, Terra *Publishing, Hertfordshire,* England.

Van der Meer F., Hecker C., Ruitenbeek F., Van der Werff H., Wijkerslooth Ch., Wechsler C., 2014: Geologic remote sensing for geothermal exploration: A review. *International Journal of Applied Earth Observation and Geoinformation* 33, 255-269.

Watkins N.D., and Walker G.P.L., 1977: Magnetostratigraphy of Eastern Iceland. *Am. J. Sci., 277,* 513-584.

Appendix

The geological map coupled to geothermal manifestations of the Grændalur valley shows a high concentration of geothermal manifestations in the subglacial hyaloclastite formation overlain by surface deposits (fig.48).

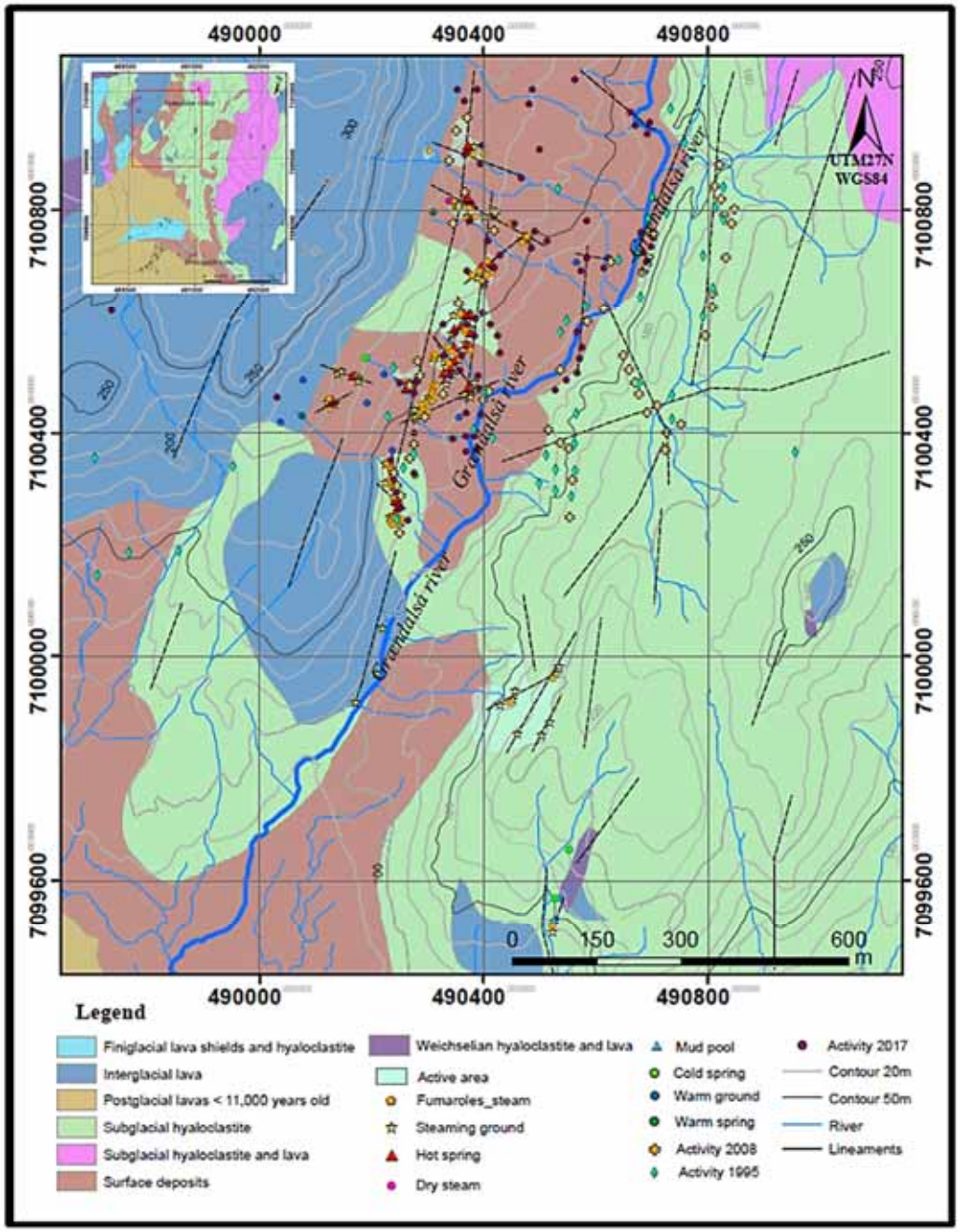

Figure 48: Geological map of Grændalur valley with geothermal manifestations.

Figure 49 shows the spatial resolution of ASTER (90 x 90m), Landsat (30 x 30m) and TIR camera (14.7 x 15.1cm) images.

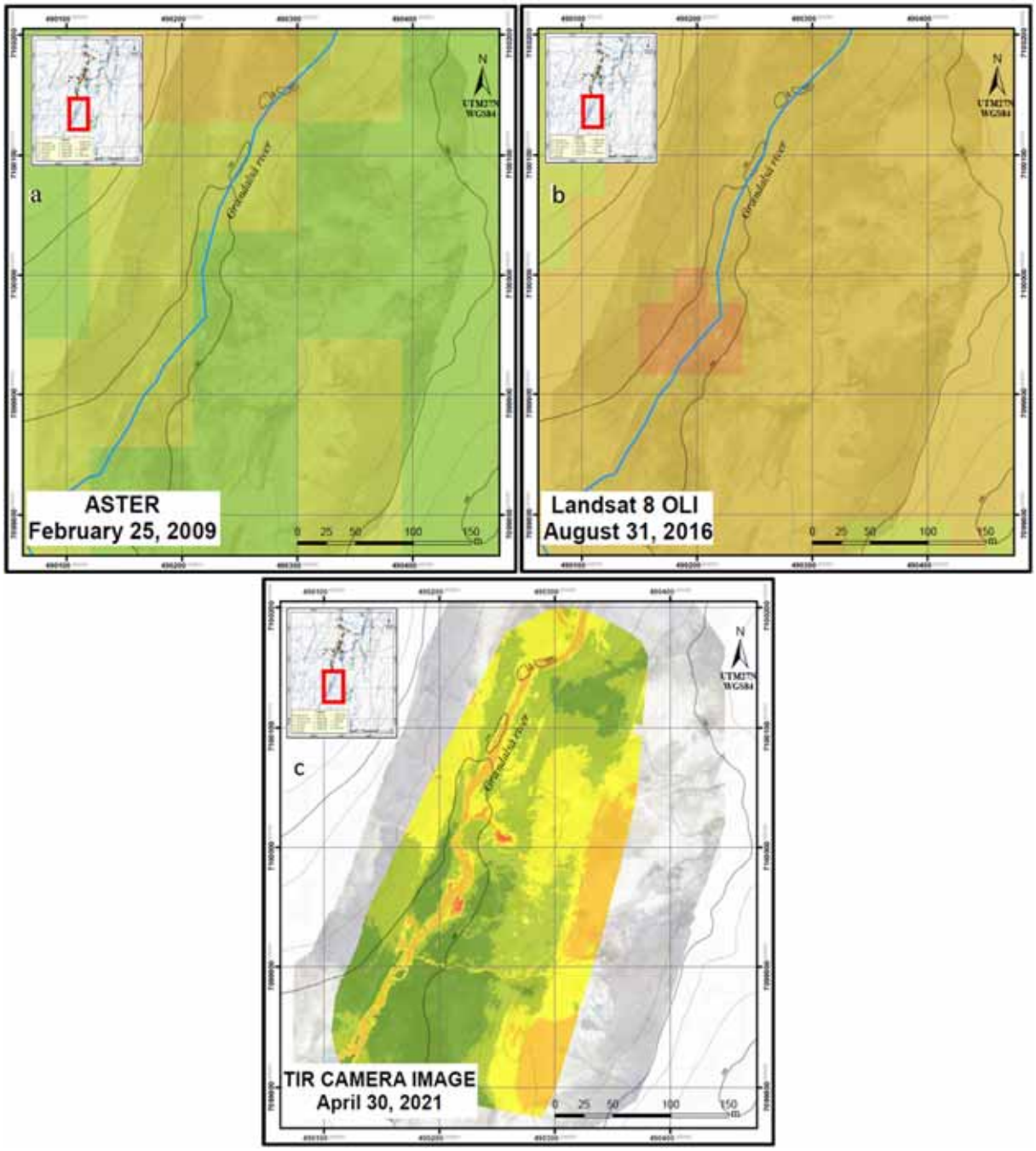

Figure 49: Spatial resolution of satellite images and the TIR camera of the southern Grændalur valley. a: ASTER image (90 x 90m), b: Landsat image (30 x 30m) and TIR camera image (14.7 x 15.1cm)

Below are the larger versions of the Grændalur valley thermal anomalies maps ranging from 2005 to 2020 shown in Figure 42.

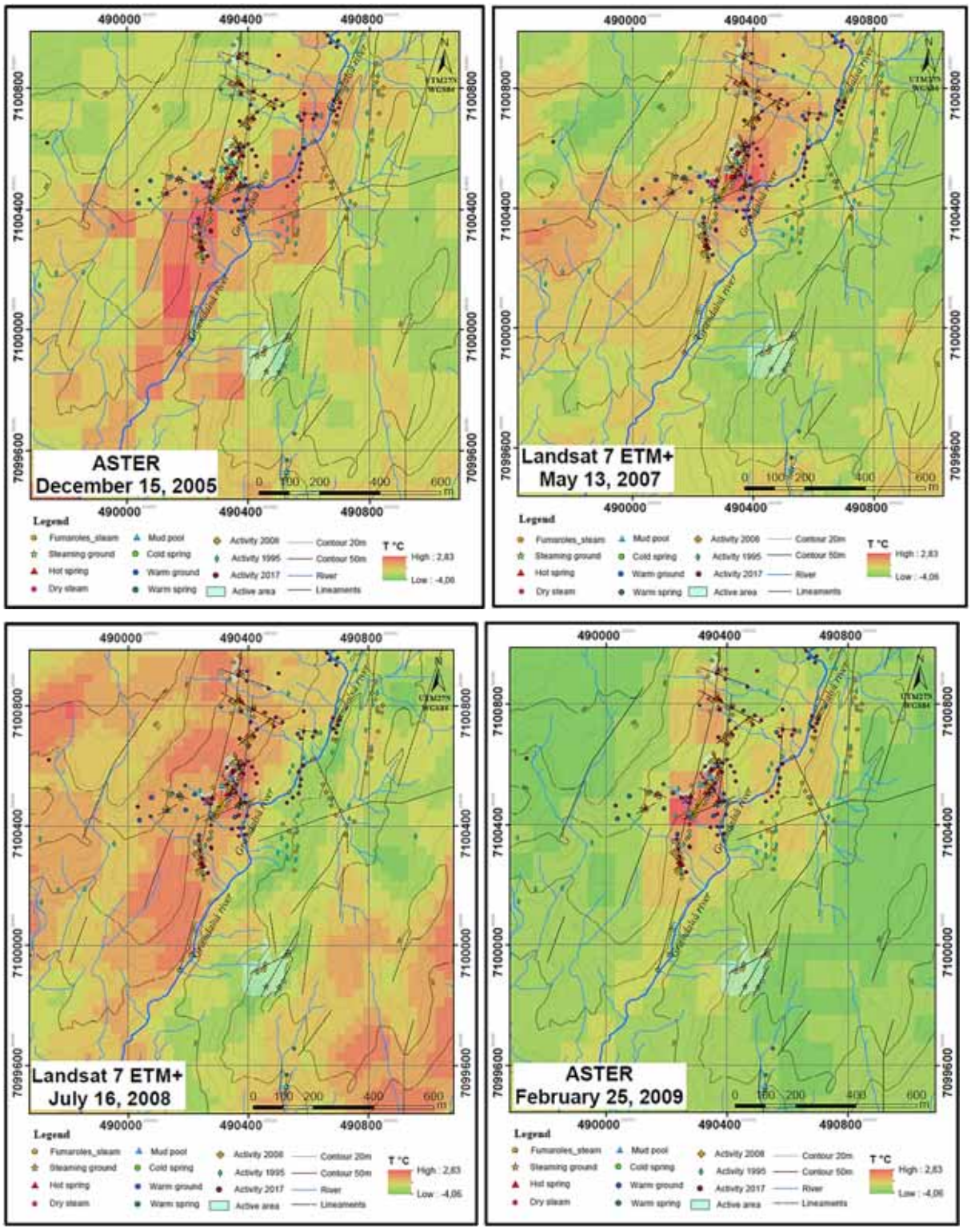

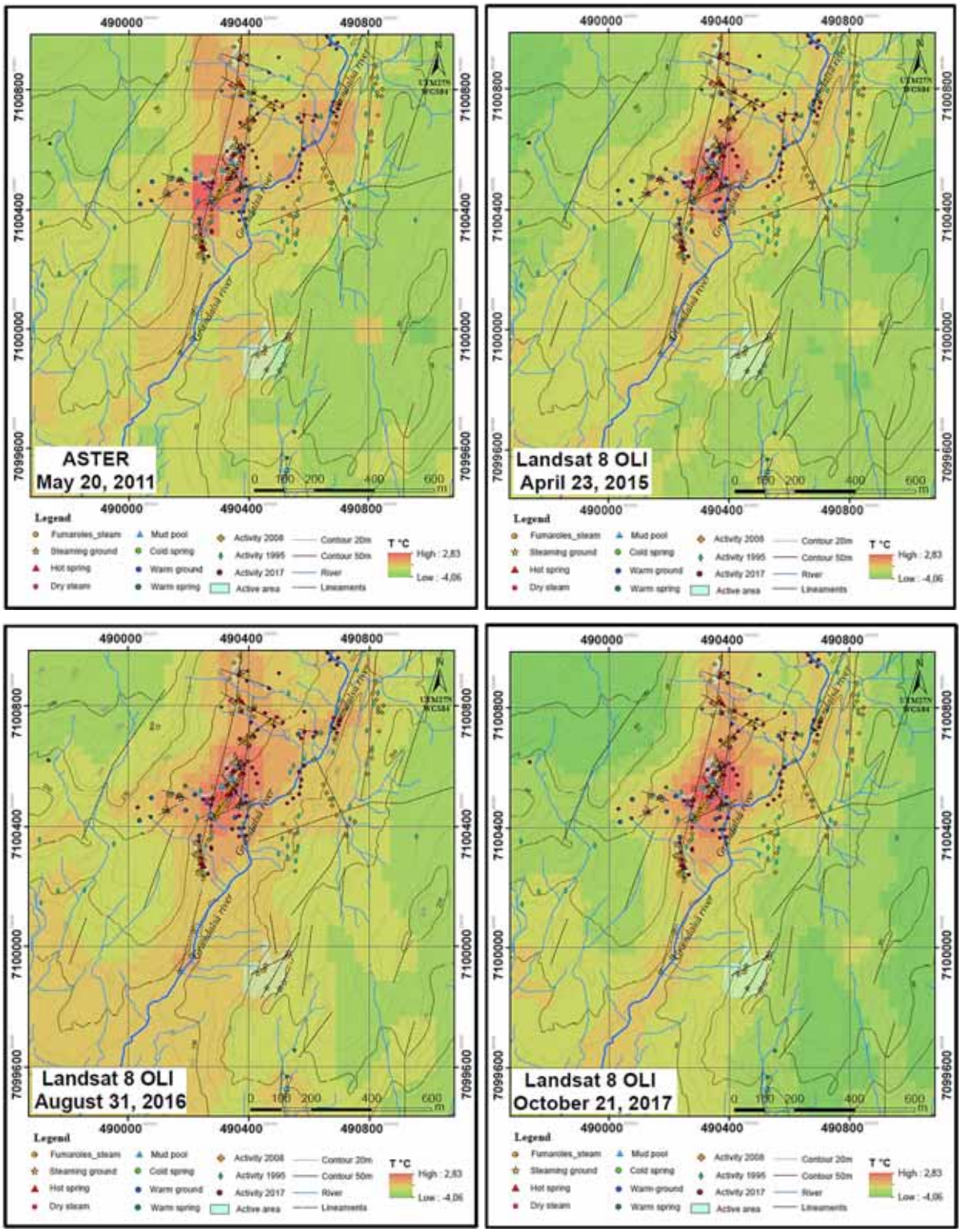
ASTER
May 20, 2011
Landsat 8 OLI
April 23, 2015
Landsat 8 OLI
August 31, 2016
Landsat 8 OLI
October 21, 2017
490000
490400
490800
7100800
7100400
7100000
7099600
Legend
Fumaroles_steam
Steaming ground
Hot spring
Dry steam
Mud pool
Cold spring
Warm ground
Warm spring
Activity 2008
Activity 1995
Activity 2017
Active area
Contour 20m
Contour 50m
River
Lineaments
T °C
High : 2,83
Low : -4,06
0 100 200 400 600
m

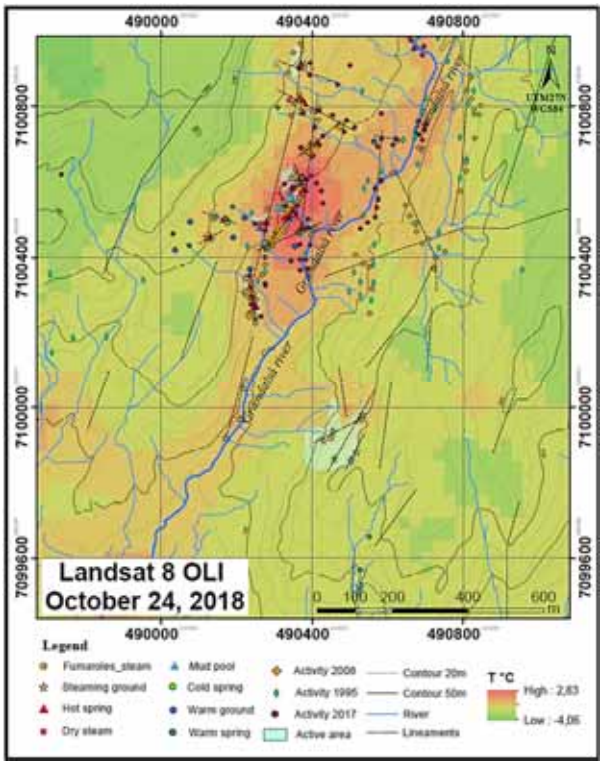
490000
490400
490800
7100800
7100400
7100000
7099600
Landsat 8 OLI
October 24, 2018
0 100 200 400 600 m
Legend
Fumaroles_steam
Steaming ground
Hot spring
Dry steam
Mud pool
Cold spring
Warm ground
Warm spring
Activity 2008
Activity 1995
Activity 2017
Active area
Contour 20m
Contour 50m
River
Lineaments
T °C
High : 2,83
Low : -4,06

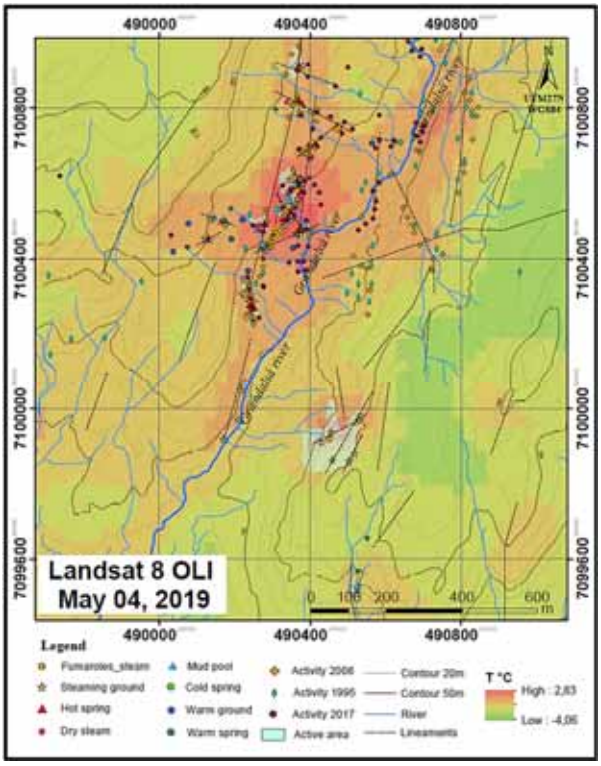
490000
490400
490800
7100800
7100400
7100000
7099600
Landsat 8 OLI
May 04, 2019
0 100 200 400 600 m
Legend
Fumaroles_steam
Steaming ground
Hot spring
Dry steam
Mud pool
Cold spring
Warm ground
Warm spring
Activity 2008
Activity 1995
Activity 2017
Active area
Contour 20m
Contour 50m
River
Lineaments
T °C
High : 2,83
Low : -4,06

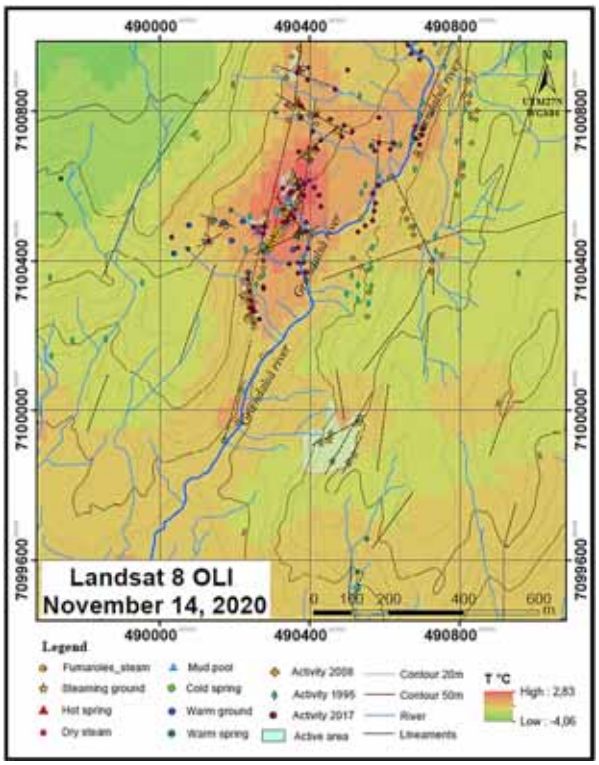
490000
490400
490800
7100800
7100400
7100000
7099600
Landsat 8 OLI
November 14, 2020
0 100 200 400 600 m
Legend
Fumaroles_steam
Steaming ground
Hot spring
Dry steam
Mud pool
Cold spring
Warm ground
Warm spring
Activity 2008
Activity 1995
Activity 2017
Active area
Contour 20m
Contour 50m
River
Lineaments
T °C
High : 2,83
Low : -4,06